Received: 15 September 2023 | Revised: 13 May 2024 | Accepted: 3 June 2024

DOI: 10.1002/nme.7552

RESEARCH ARTICLE

WILEY

Local reduced subspaces of subchannel-inspired subdomains

Shenhui Ruan | **Jorge Yanez** | **Andreas G. Class**

Institute for Thermal Energy Technology and Safety, Karlsruhe Institute of Technology, Eggenstein-Leopoldshafen, Germany

Correspondence
Shenhui Ruan, Institute for Thermal Energy Technology and Safety, Karlsruhe Institute of Technology, Hermann-von-Helmholtz-Platz 1, Eggenstein-Leopoldshafen, 76344, Germany.
Email: shenhui.ruan@kit.edu

Funding information
China Scholarship Council, Grant/Award Number: 202106050041; Framatome Professional School

Abstract

In this article, we study an update of the traditional subchannel approximation utilizing local reduced order bases. Through employing the symmetries and periodicity of a 7-pin bundle, the global domain is decomposed into numerous repeating subdomains following several dividing strategies. We locally study the reduced basis generated by proper orthogonal decomposition. We analyze the similarities, assessing the truncation error and the distance between the linear subspaces spanned by the reduced bases. We focus on the first stage of building a reduced order model, the generation of the reduced subspace, which is usually not regarded in detail in our application problem. Our assessment related to flow blockage in liquid metal-cooled nuclear reactors, a postulated high-risk accident that results in potential fuel damage.

KEYWORDS

distances between subspaces, flow blockage, local reduced basis, proper orthogonal decomposition, repeating subdomains

1 | INTRODUCTION

Nuclear reactors of generation IV are being developed to increase the safety, reliability, and sustainability of atomic power. Among the considered designs, the liquid metal cooled fast reactors (LMFRs) seem to be the most competitive designs.[1] Nevertheless, LMFR development is not free of challenges. For most LMFRs, the pitch-to-diameter ratio of fuel rods is smaller than in light water reactors. Consequently, coolant channels are narrow and more likely to be blocked.[2,3]

Jam of flow channels has unwanted consequences, resulting in a local temperature increase, both in coolant and cladding, that could even lead to the failure of the latter. Note that the local obstruction has a negligible effect on the total mass flow rate, which increases the difficulty of its detection.[4]

Thus, the necessity of investigating obstructed bundles in LMFRs has been widely recognized. The analysis includes numerical simulations performed with different methods, which have been published. These can be classified into three large categories: system codes, subchannel codes, and computational fluid dynamics (CFD).

System codes were already used to analyze and design reactors since the 1960s. They were mainly 1D analyses, often involving assumptions and simplifying the core into several channels. They were intended to investigate the responses of the whole reactor under flow blockages.[5–7]

The next generation of software development, involved the *Subchannel codes*, which utilize a coarse discretization to model the reactor core. Consequently, they were adopted to investigate the effect of parameters with limited computational cost. They were able to predict the flow and temperature distribution in steady state and transient conditions.[8–10] However, their low spatial resolution prevents them from obtaining accurate flow behavior. They also use simplified governing equations that cannot resolve many thermal hydraulic phenomena. Empirical *ad hoc* models based on experiments are required to complement the formulation.[11,12]

In spite of their shortcomings, subchannel codes can be considered the workhorse with which most existing reactors were assessed in the 1970s and 1980s. However, their drawbacks led the research community to turn to more modern techniques, inspiring us to carry out this work.

In the *CFD* approach, one constructs a full order model (FOM) to simulate the flow and heat transfer with high fidelity.[10,13,14] However, this exactness comes with nuisances: CFD is numerically intensive. This characteristic often makes conducting a large parametric study infeasible. This situation is even aggravated due to the computational requirements for the simulation of reactor fuel assemblies, which are exceptionally high.[3,15,16] Accuracy requirements can only be satisfied by generating a detailed geometrical representation of the domain. This implies the exact modeling of small structures on a large model. Of particular importance are thin wires wrapped around the rods. This increases the difficulty of generating a high-quality mesh.

Performing FOMs with CFDs for a wide range of parameters is often prohibitively expensive. Therefore, alternative methodologies have been developed to overcome this difficulty. Among them, for its relevance in our study, we may mention reduced order models (ROMs). Compared to FOMs, ROMs are more efficient in simulating the dynamics of thermal hydraulic systems. Nevertheless, ROMs are not self-standing methodologies. High-fidelity simulations should be performed and post-processed to construct a ROM. However, once ROM is available, simulations can be carried out cheaply with high accuracy. This makes the approaches prone to carry out extensive parametric studies and uncertainty quantification.[17–20]

ROMs can be constructed by diminishing the degrees of freedom of a problem. Throughout the available techniques employed to carry out such a task, we note that the reduced basis method, which can generate optimized vector spaces with restricted dimensions, is a well-established procedure.[21] Among reduced basis procedures to obtain reduced bases of large datasets, Proper orthogonal decomposition (POD) has become a widely used method over the last decades.[22–29] In conjunction with (Petrov-)Galerkin projection, it has been successfully applied to compute reduced bases and build corresponding ROMs.

Regarding the treatment of the geometrical space, reduced basis methodologies can follow global or local approaches.[30] In global formulation, the reduced basis is obtained to optimally capture the dominant flow patterns in the whole domain. In contrast, the local technique decomposes the whole domain into parts, where a series of reduced bases are constructed. In both cases, the singular value decomposition (SVD) method[30,31] or the greedy-type algorithms[32–34] can be employed to construct bases. Among the advantages of the local technique, one may mention its improved ability to represent partial patterns. This translates into the basis with vectors of lower dimensions.[32] Global approaches require larger reduced spaces, higher computational power, and storage.

Local strategies, often regarded as less sound in the past, are nowadays a relatively mature method adopted in many investigations. A general review in which generalized information on the topic has been gathered in Reference 35. In the following discussion, we will involve the concept of so-called *archetype* components, which are used in the partitioning of geometries. These are paradigmatic patches or pieces that can be used to represent all other subdomains and to assemble the whole domain. The definition of partition is not unique and varies depending on the model problem. In the literature, we have identified two main strategies to achieve the localized approach. They regard the way in which the high resolution calculations are performed and how the snapshots are collected.

1. The first strategy considers global high fidelity results. Those are then split into partitions with different sizes and shapes. The dimension reduction procedure is then applied locally. Thus, each part is associated with its own reduced basis. Henceforth, the ROM is built up coupling multiple patches and minimizing discontinuities at subdomain interfaces.[31,36–40]
2. The second approach involves dividing the total domain into pieces from the beginning. This approach assumes that some symmetries, similarities and so forth exist in the domain, which can be assembled with a few types of archetype parts. The FOM calculations are performed in the archetypes –one or a few subdomains–, in which the snapshots are also gathered. The rest of the domain is disregarded. ROM is then built by standard techniques. Nevertheless, continuity constraints or parametric boundary conditions are imposed to combine the multiple local ROMs.[41–47] This

approach only requires local high fidelity solutions to generate the reduced spaces, which boosts the efficiency of the process. However, extra considerations of the interface conditions increase the complexities.

In this article, we will consider a third procedure, in which we will base our investigation. It combines the ideologies of the aforementioned two treatments to construct the reduced basis. Our physical model, the fuel assembly of an LMFR consists of repeating parts and has symmetries, and can be reconstructed considering a few archetype subdomains. We will extract local snapshots from global FOM solutions and generate the corresponding reduced basis for each type of subdomain. Note that this local approach can be advantageously utilized for our peculiar geometry. Besides, it is not novel. It was recently applied in some investigations.[48–50]

Conceptually, for a periodic and symmetric geometry, the domain decomposition adopted to construct the local reduced basis is an approach not far from the mindset utilized in developing subchannel codes, where the division of the global domain was also an essential issue. Still, there are remarkable advantages to using a reduced basis method. Note that the subchannel approach was also commonly referred to as a *Lumped* parameter model.[11,12] As its name indicates, the technique implies that an area is divided into homogenized and symmetric control volumes (also called subchannels). In each of them, only one single value is defined and spatial gradients of variables do not exist. The method was reasonable at a time contemporary with the development of early computers when hardware soon reached its limits. It allowed us to bring computational analysis to guide the design of nuclear cores.

Nowadays, increasing computing power allows researchers to follow more subtle approaches. Thus, adopting, in some sense, the ideology of the subchannel method does not mean renouncing to consider spatial gradients. The usage of a reduced basis extracted in a small domain –channel– from a high fidelity solution allows to consider few values per domain –order of ten– while keeping an accurate flow description.

Periodicity and symmetry also allow us to expect that the dominant flow features under different conditions are very close in different locations. In mathematical terms, we are approximating a flow in subdomains by subspaces spanned by reduced bases. Therefore, *similarities* between flow patterns should translate into closeness among the reduced subspaces. A concept that can be characterized by the distances between subspaces.

Distance and metrics are classical mathematical notions that have been amply generalized to characterize a vast type of systems. Its encyclopedic review, involving their characteristics and properties, can be found in Reference 51. In this research, we are particularly concerned by the methods adopted to measure the distance between linear subspaces.

In this regard, we are actually interested in examining a reduced subspace of dimension k inside a high dimensional -fidelity- subspace of dimension n. The distances we may wish to quantify are those among different local reduced bases, arising from different locations or simulations, of similar -but not forcefully equal- dimensions k and $k' \ll n$.

The level of abstraction, in which the similarity in the local reduced basis is characterized by the distance among the reduced subspaces of each piece, has many advantages. Particularly, it allows us to apply the existing theory of distances among subspaces. In this regard, we need to mention the fundamental concept of the *Grassmann manifold*[52–54] to provide a general frame to measure distances between linear k-dimensional subspaces included in a n-dimensional one.

Inside this theoretical environment, several definitions of distance exist to measure the similarities among subspaces for both equi-dimensional and non-equi-dimensional cases. A comprehensive review can be found in Reference 53. The different expressions are due to heterogeneous conceptual approaches to consider the measurement. Their concrete description will be addressed in detail in Section 4.

This article is devoted to analyzing the local reduced bases, including their potentiality and differences. In frames of a contemporary subchannel-inspired approach to nuclear engineering, the flows consist of repetitive pieces with symmetries. Thus, we study the possibility of creating a generic subdomain-level reduced basis to approximate high-fidelity solutions of cases varying in physical conditions. In addition, some factors, including the effect of domain decomposition strategies, are considered.

To achieve this goal, we first describe the simulations performed on which we base our analysis in Section 2. In Section 3, we describe the POD vectors characterizing their capability of reproducing the calculations by the truncation error of the reduced basis. Finally, in Section 4, we address the problem in terms of distances among subspaces.

2 | HIGH FIDELITY SIMULATIONS

2.1 | Physical model

The flow domain utilized in this study is a 7-pin bare rod bundle arranged in a hexagonal array, see Figure 1. The working fluid, liquid lead-bismuth eutectic (LBE), is bounded by bundle walls, marked in green. The flow moves along the longitudinal direction. The geometrical parameters of the bundle correspond to the ones studied in the experiments of Reference 4. A bundle consists of seven rods with a diameter of 8.2 mm and a length of 300 mm. The rods are arranged with a centroid pitch of 10.49 mm and a wall rod pitch of 10.58 mm equivalent to a hydraulic diameter of 6.52 mm.

High-fidelity simulations were carried out employing incompressible Reynolds-Averaged Navier–Stokes (RANS) equations. All the calculations were steady-state and performed using an OpenFOAM solver, SimpleFoam.[55–57] This procedure is especially suited for incompressible turbulent flow.

To close the RANS equations, we selected the standard $k-\epsilon$ model[58,59] to account for terms corresponding to turbulence. The standard wall function[58] was involved to represent the flow in near-wall regions.

The effect of blockage is an important point for this research. It is characterized as a porous medium, for which the detailed simulations are complicated. Hence, we chose the Darcy-Forchheimer law to model that region. The hydraulic resistance is thus approximated as an additional source term in the momentum equation. The model has been widely used due to its potential for flow simplification.[60,61]

The bundle mesh is displayed in Figure 2. To attain reasonable solutions, the grid should satisfy some requirements. Recall that the standard $k-\epsilon$ model and standard wall function are adopted. Therefore, the size of the first layer of cells ensures that y^+ is around 60.[58,59,62] For cells further away from the wall, a slightly larger thickness is adopted. Moreover, the aspect ratio –the ratio of the longest to the shortest edge– should be maintained in a suitable range,[63] which is taken to be about 5.5—the maximum. To verify the constraints mentioned above, a structured hexahedral mesh with 806,400 cells was employed in the simulations.

2.2 | Subdomains

As mentioned in Section 1, the fundamental idea of subchannel codes lies in dividing the total domain into sub-pieces.[11] One of those divisions is displayed in Figure 3, including inner, edge, and corner sub-blocks. Such is similar to the local

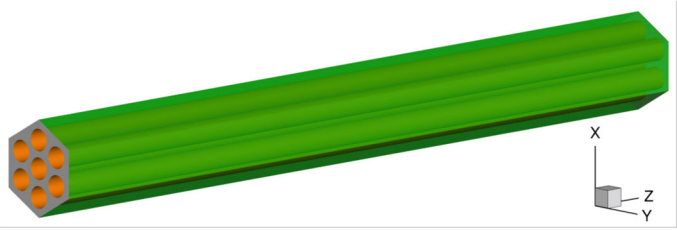

FIGURE 1 Tube bundle layout.

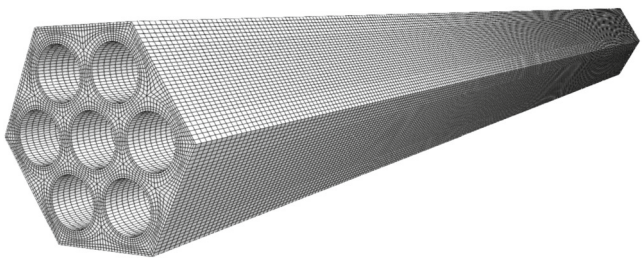

FIGURE 2 Mesh employed.

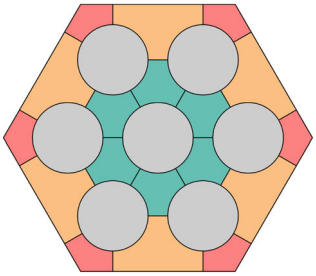

FIGURE 3 Divisions of the 7-pin tube bundle; green: Inner subchannel; orange: edge subchannel; red: corner subchannel; gray: rod.

TABLE 1 Domain decomposition strategies.

Strategy	Pieces	Figure	Pieces	Num. cells
1	3	Figure 4	Ω_{1a}	200
			Ω_{1b}	900
			Ω_{1c}	540
2	3	Figure 5	Ω_{2a}	1200
			Ω_{2b}	2200
			Ω_{2c}	1080
3	1	Figure 6	Ω_3	4480
4	1	Figure 7	Ω_4	8960

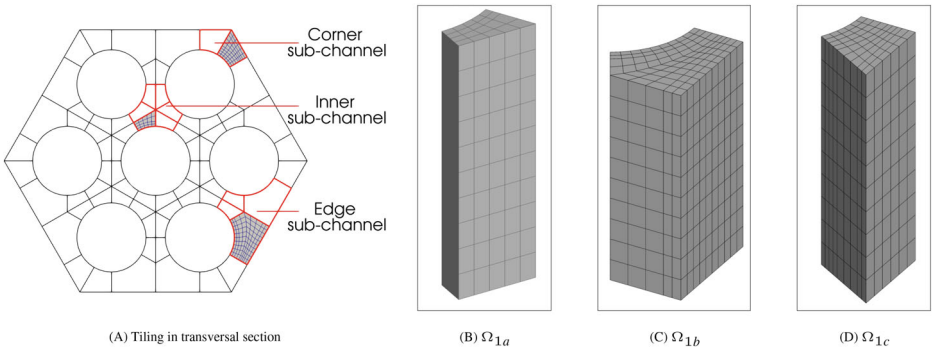

FIGURE 4 First decomposition strategy: (A) Strategy adopted; (B)–(D) Subdomains.

domain decomposition applied in POD and reviewed above. In both cases, the tiling is based on a geometrical structure showing symmetries like the bundle in Figure 1.

The division into repeating parts is not unique and may influence the performance of the POD basis (as did in subchannel codes). To investigate that impact, four decompositions are applied, see Table 1. In all cases, based on the experience gained utilizing subchannel codes[9,64,65] and with the aim of simplifying our study, we assigned a single length of all subdomains set to be 10 mm.

In the first strategy, the whole bundle can be built utilizing three subdomains, Ω_{1a}, Ω_{1b} and Ω_{1c}, Figure 4. From the figure, we can observe that an inner subchannel consists of six Ω_{1a}; an edge subchannel contains two Ω_{1a} and two Ω_{1b}; and a corner subchannel is the makeup of two Ω_{1c}.

The second strategy follows the same ideology as the subchannel codes, see Figure 5. The Ω_{2a}, Ω_{2b} and Ω_{2c} are applied to construct the global domain.

Larger parts are employed in the third and fourth strategies. For the third decomposition strategy, Figure 6, the domain Ω_3 contains an inner and edge subchannels and two halves of a corner subchannel. Ultimately, the fourth strategy utilizes the largest elements. Element Ω_4 of Figure 7 is the makeup of two duplicate Ω_3.

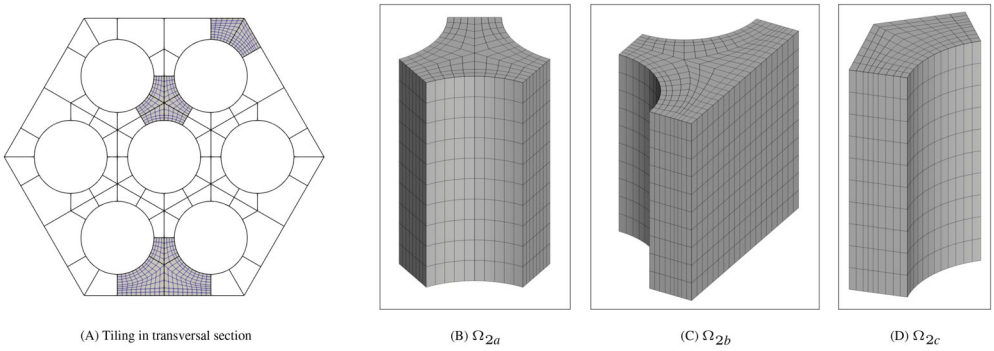

FIGURE 5 Second decomposition strategy: (A) Strategy adopted; (B)–(D) Subdomains.

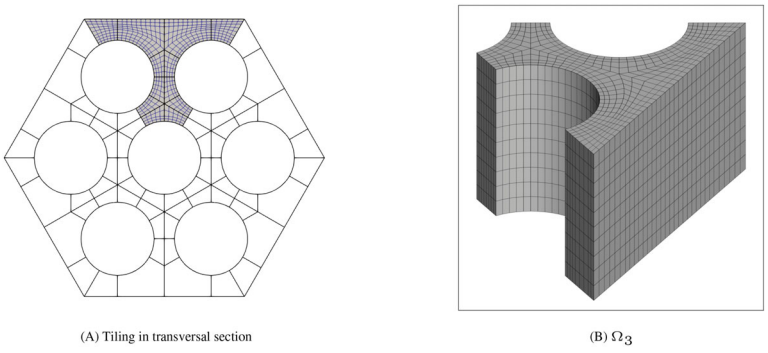

FIGURE 6 Third decomposition strategy: (A) Strategy adopted; (B) Subdomains.

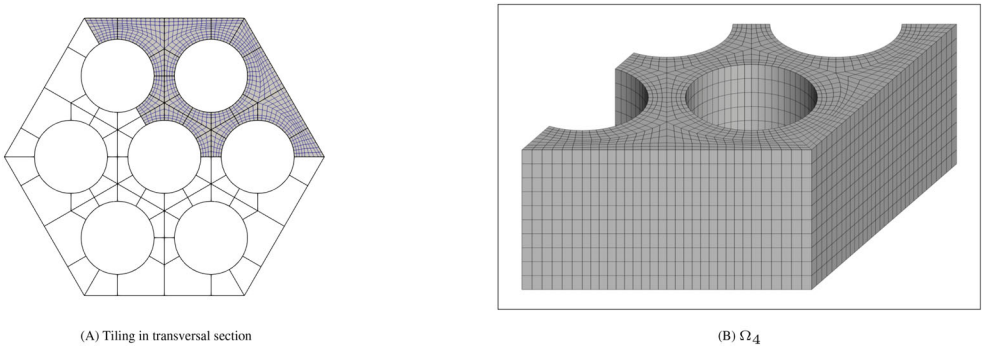

FIGURE 7 Fourth decomposition strategy: (A) Strategy adopted; (B) Subdomains.

2.3 | Simulation setups

The physical model and simulation methods shown in previous sections should be completed with adequate physical setups. In the approach followed, heat transfer was overall neglected. The imposed momentum boundary conditions are listed below.

In the inlet, zero pressure gradient $\partial_n p = 0$ and a prescribed velocity $\mathbf{u} = \mathbf{u}_{in}$ was imposed. Velocities adopted can be seen in the third column of Table 2. In the outlet, zero velocity gradient, $\partial_n \mathbf{u} = 0$, and zero pressure $p = 0$ were defined. Finally, bundle and tube walls were regarded as impermeable. Also, zero pressure gradient $\partial_n p = 0$ and the no-slip boundary condition was imposed.

Concerning the fluid properties, lead-bismuth eutectic at 493 K, is characterized[66] by a density $\rho = 10427.6\,\mathrm{kg\,m^{-3}}$ and by a dynamic viscosity of $\mu = 2.2 \times 10^{-3}$ Pas.

TABLE 2 Physical conditions of FOM simulations.

Case No.	Blockage	Inlet velocity [m/s]	Profile
1	None	1.74	Uniform
2	None	1.74	Fully developed
3	None	1.0	Uniform
4	Figure 8A	1.74	Uniform
5	Figure 8B	1.74	Uniform
6	Figure 8C	1.74	Uniform

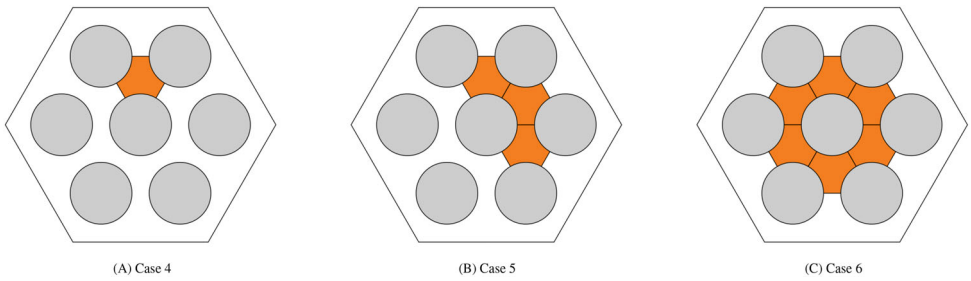

FIGURE 8 Transversal section at half-length. Blockage for Cases 4, 5, and 6.

Six steady state FOM simulation cases are listed in Table 2. They intend to study the influence of two effects: inlet boundary conditions (Cases 1, 2, and 3) and blockage (Cases 4, 5, and 6).

Let us consider Case 1 as a base case. A uniform inlet velocity of $1.74\,\mathrm{m\,s^{-1}}$ was adopted. That corresponds to the maximum mean flow rate used in an experimental study.[4] Case 2 regards a fully developed flow distribution. Its mean speed is equal to case one. Its goal is to study the influence of flow distribution at the inlet. Case 3 was performed to investigate the effect of the inflow magnitude.

The second group of simulations (4, 5, and 6) were conducted to reveal the impact of flow impediment. Simulations regard three cases with different numbers of obstructed inner subchannels displayed in Figure 8. The blockage is of the same size as the subdomain Ω_{2a} with a length of 30 mm (see Figure 5). It is longitudinally located in the middle of the bundle. The Reynolds number for an inlet velocity of $1.74\,\mathrm{m\,s^{-1}}$ is 6.0×10^4. For Case 2, where the mean inflow is $1.0\,\mathrm{m\,s^{-1}}$, the value is 3.4×10^4. Hence, all simulations are turbulent according to empirical correlations proposed by Cheng and Todreas.[67]

2.4 | Results and analysis

The simulations were validated by comparing the pressure drop results against the well-known correlations of Blasius[68] and Cheng and Todreas.[67] They showed excellent agreement with these references.

For the investigation reported in this article, it is important to discuss some results concerning the velocity distribution significantly downstream. Therefore, we study it near the outlet and in the neighborhood of the blockage.

Figure 9 shows the scaled velocity magnitude, *Umag*, in a transversal section of the outlet for all six cases. The absolute velocities are scaled by dividing the constant inlet values of each configuration, see Table 2. Although the inflow condition is different, the scaled profiles at the outlet for Cases 1, 2, and 3 are nearly equivalent. Regardless of the inflow conditions of Case 1, at the channel exit, the flow field becomes almost fully developed and thus very comparable to Case 2. Case 3, in which inflow is lower, shows a re-scaled velocity profile of Case 1.

Blocked cases (4, 5, and 6) show a dissimilar pattern. The velocity in the blocked subchannels remains much lower than in the previous cases. This happens even considering that the outlet is relatively far away from the blockage (130 mm).

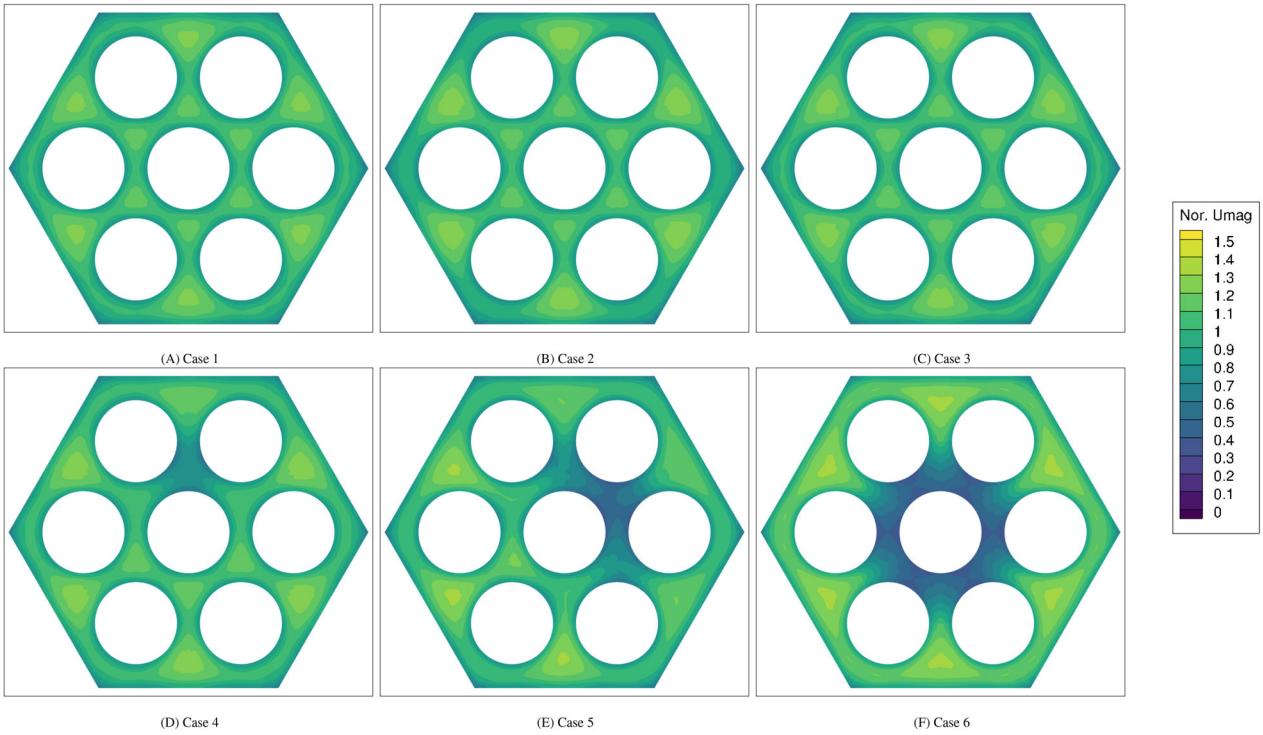

FIGURE 9 Scaled velocities magnitude (divided by the constant inlet values of each configuration, see Table 2). Transversal cuts at the outlets.

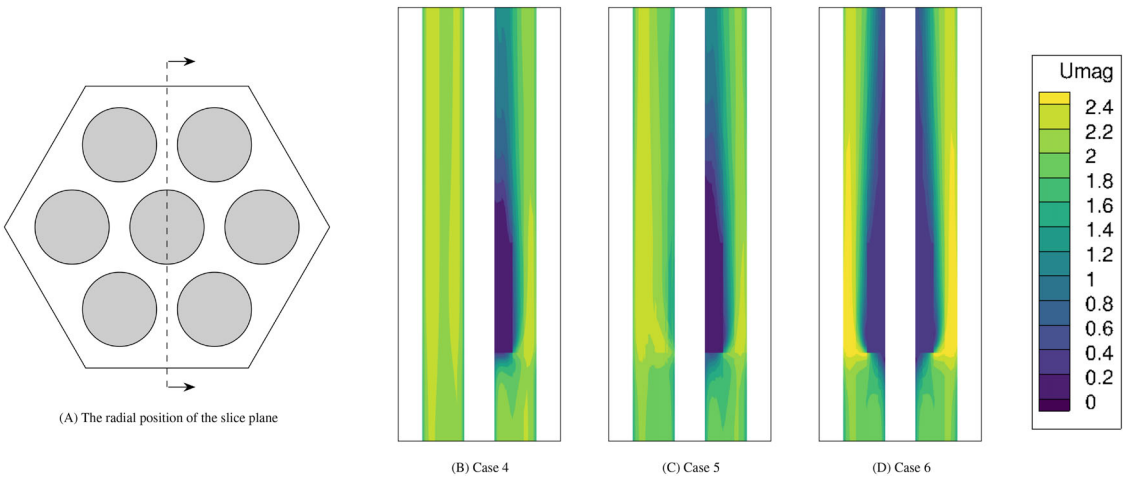

FIGURE 10 Longitudinal cuts of velocity profiles near the blockage for Cases 4, 5, and 6. The axial range of the cut is from 110 to 240 mm, measured from the inlet plane.

Fluid speed in neighboring subchannels is also smaller than in Case 1. In contrast, motion in the edge and corner subchannels is relatively higher.

The velocity distribution near the blockage is displayed in Figure 10. The longitudinal location of the cut ranges from 110 to 240 mm, measured from the inlet plane. The results indicate a low-velocity region upstream of the obstruction. This region could be characterized by poor heat convection. The jam significantly affects flow velocity, creating an area of low motion even far away from there. Indeed, a larger blocking area leads to a more substantial low-velocity region near the blockages, especially downstream.

3 | POD AND REDUCED BASIS

3.1 | Snapshots and POD

By performing a simulation on FOMs, we obtain high-fidelity discrete solutions of different variables (e.g., velocity and pressure). We carry out i cases differing in physical settings. The results can be stored in a matrix, $S \in \mathbb{R}^{M \times n}$, composed of M vectors $u_1, \ldots, u_M \in \mathbb{R}^n$ called snapshots. In this research, we treat each variable separately. n corresponds to the dimensions of the physical subdomain, aka the number of cells. Note that the original *snapshot* indicates a state vector, that is, the FOM solution, of a system at a particular time.[69] In our study, a set of steady state data were gathered. The states restricted in subdomains were extracted. Therefore, the snapshots considered in this article denote *geometric snapshots* and/or *spatial snapshots*.

One of the main goals of this study is to extract flow features in subdomains. Thus, M can have different meanings for the decomposition strategies already mentioned in Section 2.1. The domain is decomposed into m repetitive regions. We may treat the i simulations in two different ways. We may regard them individually (see Figure 11, each vector of the matrix represents the high fidelity solution in a subdomain for an individual case), in which case $M = m$, or alternatively, multiple simulations can be gathered so that $M = i \times m$. An example of the matrix gathering the snapshots for two cases is shown in Figure 12, where the $M = 2 \times m$. The matrix has two sub-blocks, each containing m snapshots for Cases 4 and 5, respectively. Remark that we performed several simulations and utilized different domain division strategies. Therefore, many case- and subdomain-specific snapshot matrices were collected.

In this research, POD employing the SVD algorithm was adopted to build a reduced basis. Note that we generated various reduced bases with respect to the aforementioned case- and subdomain-specific snapshot matrices. The POD

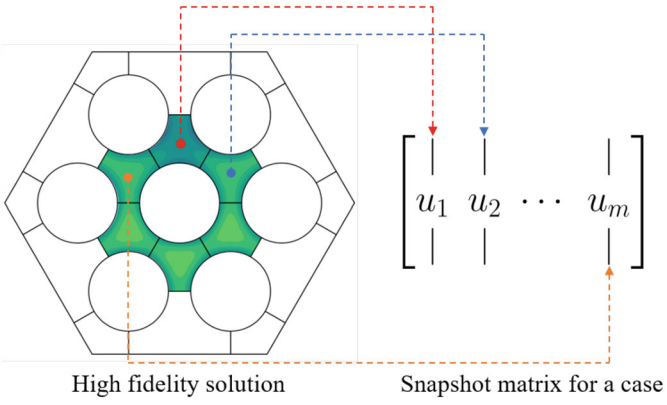

FIGURE 11 Matrix ($S \in \mathbb{R}^{M \times n}$, where $M = m$) containing snapshots, $u_1, \ldots, u_m \in \mathbb{R}^n$, for an individual steady state case.

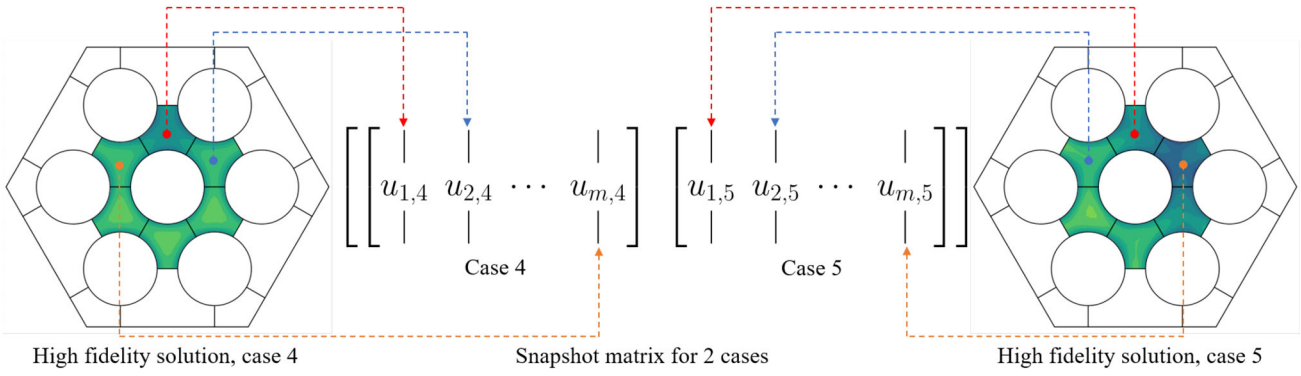

FIGURE 12 Matrix ($S \in \mathbb{R}^{M \times n}$, where $M = 2 \times m$) containing snapshots, $u_{1,i}, \ldots, u_{m,i} \in \mathbb{R}^n$ (where i is 4 or 5), for two steady state cases, that is, Cases 4 and 5.

basis, defined as Φ, obtained by the span of the first N reduced basis vectors is the best N-dimensional approximation of the snapshot matrix S.[70]

The percentage of energy corresponding to the neglected $M - N$ vectors is denominated *truncation error* ε.[70,71]* This magnitude can be computed in terms of the sum of the squares of the $M - N$ singular values, σ, as

$$\varepsilon = \frac{\|S - \Phi\Phi^T S\|_F}{\|S\|_F} = \frac{\sqrt{\sum_{j=N+1}^{M} \sigma_j^2}}{\sqrt{\sum_{j=1}^{M} \sigma_j^2}}, \tag{1}$$

where $\|\cdot\|_F$ denotes the Frobenius norm of the matrix.

In many engineering practical cases, singular value decay is exponential, guaranteeing a few POD modes to achieve a high energy threshold.[35] Thus, ε constitutes a criterion to select N.

3.2 | Reduced basis and truncation error

In this research, snapshots were sampled from the six high-fidelity simulations. In terms of geometry, sampling included all the subdomains except those in the area of the blockage. Figure 13 displays iso-surfaces of the first four modes of axial velocity in the inner subchannel obtained from Case 1.

We may analyze the shapes of the vectors. Without blockages (Figure 13), the fluid flows alongside the axial direction freely. Therefore, variations are mainly due to wall friction and are thus small in the longitudinal direction. This physical behavior is captured by the first and second modes, where iso-surfaces mimic distances from the walls. Vectors one and two are reciprocal. Variations not determined by distances to the walls are set aside for higher orders. Changes in the direction perpendicular to the walls are accounted for by the third vector. Secondary currents are only included in the fourth mode.

Configuration of the basis vectors in Case 5 is significantly affected by the existence of blockages (Figure 14). Like in Case 1, the pattern of the first basis vector is still governed by axial motion. Nevertheless, its shape no longer mimics strictly wall distance. Changes in the wall-normal direction start appearing in the second and third modes. These changes are induced by the low-velocity region downstream of the obstruction, in agreement with the characteristics already shown in Figure 10. Finally, the fourth basis vector is strongly influenced by stagnant areas upstream of the blockage. The notable gradient in the longitudinal direction is due to this issue. Secondary channel currents are relegated to higher modes.

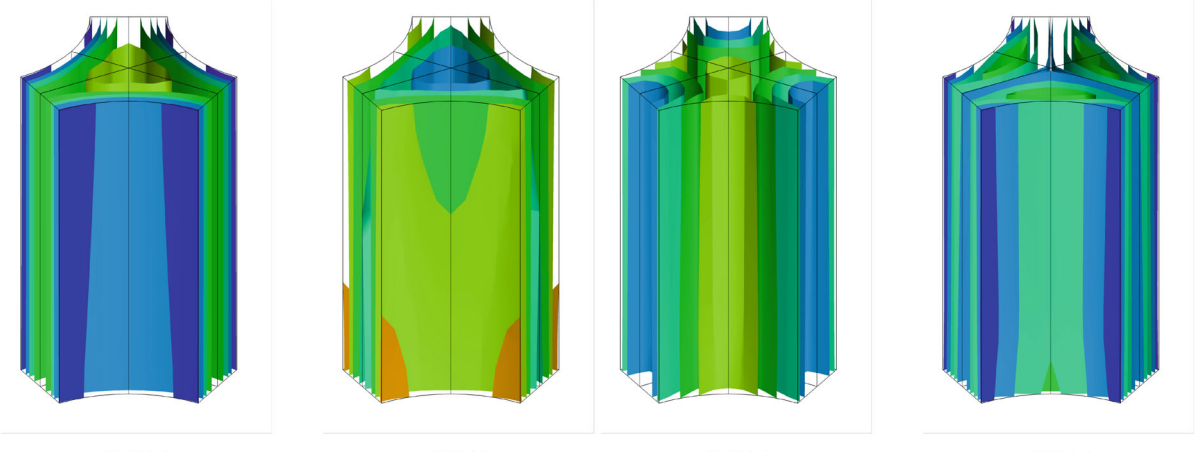

FIGURE 13 Iso-surfaces of the first four velocity basis vectors for Case 1. Shown is the longitudinal component U_z in Ω_{2a} domain (see Figure 5B).

3.3 | Truncation error

Reduced basis retains only the first N vectors. This induces a dissimilarity that we denote truncation error, Equation (1). This magnitude is an essential criterion to qualify the suitability of an approximation basis, measuring its capacity for reconstructing the fields. Note that we computed respective reduced bases for each type of subdomain whose shapes were displayed in Section 2.2. In the following figures, the results are shown as a function of the number of vectors of the basis. That means for an archetype partition, for example, Ω_{1a}, the same amount of vectors are utilized to truncate every Ω_{1a}-type subdomain. In addition, we expected the division strategies to affect the percentage of neglected flow energy.

The truncation error of the small subdomain Ω_{1a} and the subchannel one Ω_{2a} is presented in Figure 15. For unblocked cases (1, 2, and 3), only a few modes are necessary to reproduce the flow features. This is due to the simplicity of the flow field and the symmetries existing in the channel. For cases with obstacles (4, 5, and 6), blockage leads to significant local variations of the motion. The number of modes required to reach the same accuracy increases dramatically. See that flow complexity was already noted in Section 3.2. Notably, this resulted in more complicated basis vectors (compare Figures 13 and 14). However, even in blocked cases, 20 modes are enough to retain more than 99% of the energy of the original flow field.

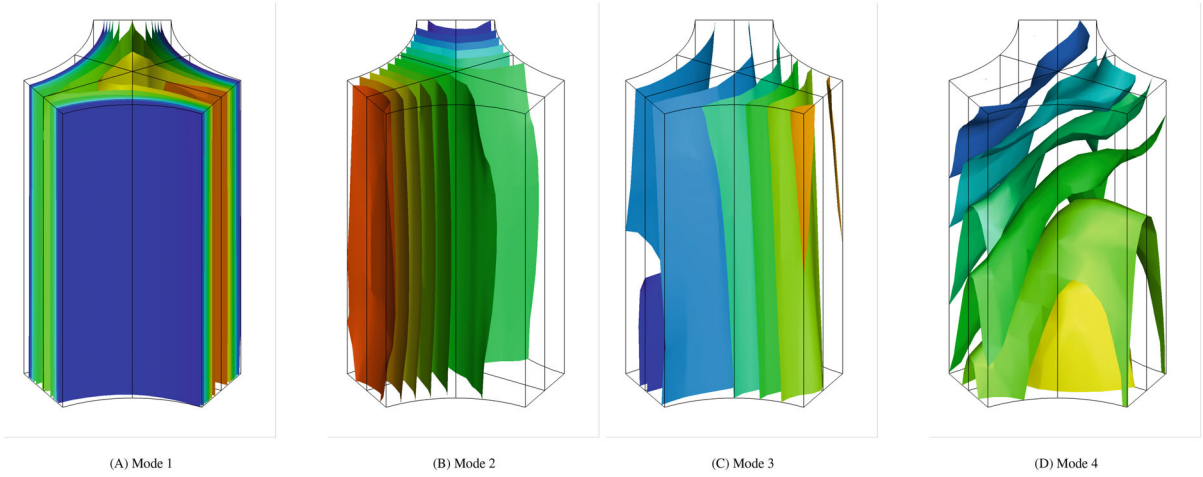

FIGURE 14 Iso-surfaces of the first four velocity basis vectors for Case 5. Shown is the longitudinal component U_z in Ω_{2a} domain (see Figure 5B).

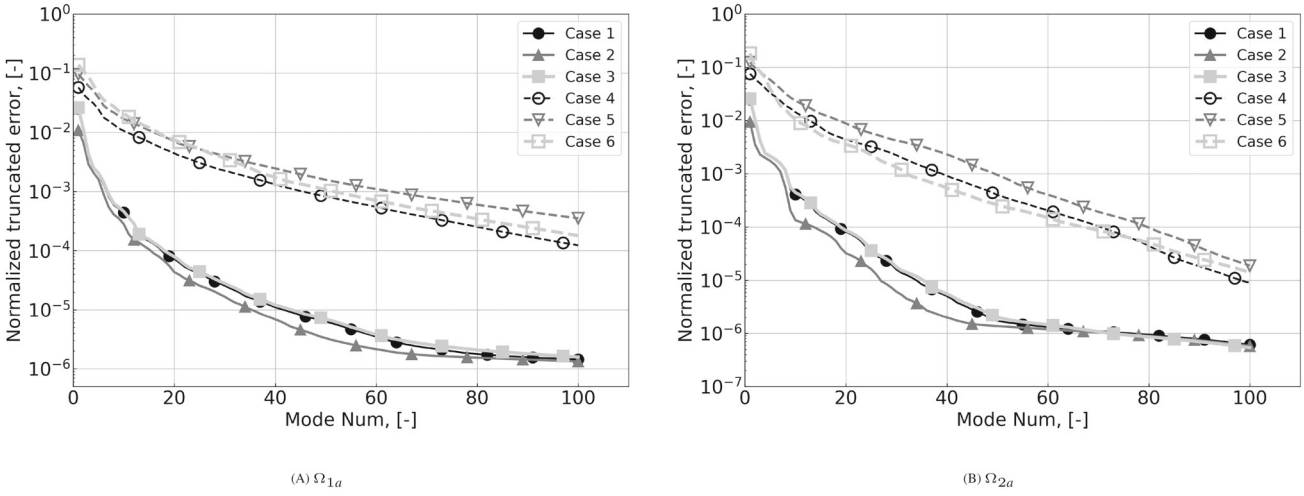

FIGURE 15 Truncation error ε of the velocity in Ω_{1a} and Ω_{2a} of all cases.

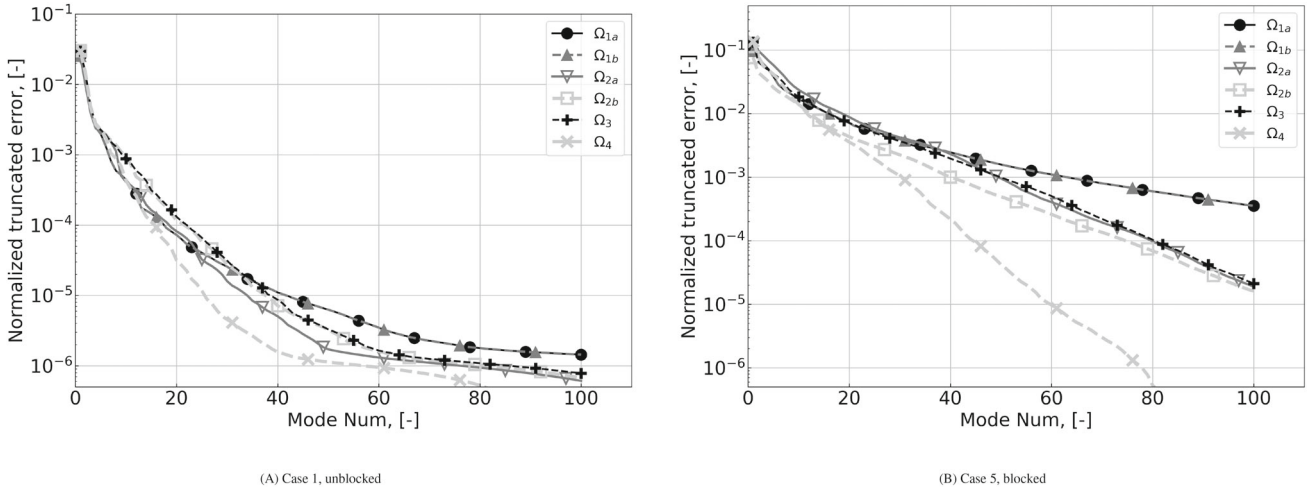

FIGURE 16 Comparison of truncation error ϵ of the velocity for (A) unblocked and (B) blocked problems.

Results above reveal that errors in Ω_{1a} and Ω_{2a} are not the same. The error in subdomains built by four strategies (as listed in Table 1) is presented in Figure 16A, which reveals that error descends exponentially with N, the number of basis vectors. This trend is similar in different subdomains. In this unblocked case, considering 20 modes decreases the error to the order of 1×10^{-4}, a very low value for most applications.

Compared to the case of Figure 16A, the decay of the obstructed case of Figure 16B is two orders of magnitude slower. The trend is similar in different subdomains, except Ω_4, which experiences a drastic decay.

The location of the subdomains influences the error registered. Note that obstructions are exclusively located in the inner subchannel. This leads to a larger truncation error in domains Ω_{1a} and Ω_{2a} than in Ω_{1b} and Ω_{2b}. Remark the relative location and geometrical pattern of the subspaces shown in Figures 4 and 5.

We may now expand our analysis to find out the geometrical 3D distribution of error, ϵ_{3D}. It is a field whose element contains a relative truncation error for each cell. Analogously to Equation (1), we define the 3D error as

$$\epsilon_{3D} = \left|(I - \Phi\Phi^T)S\right| / |S|, \tag{2}$$

where S is a snapshot matrix and Φ is a matrix containing the reduced basis vectors. The Φ is directly computed using POD for S, indicating the 3D contour is reproduced by its own reduced basis. The $|\cdot|$ and $/$ are element-wise absolute value and division operators, respectively.

Note that the whole geometry is assembled by several types of partitions, for example, Ω_{1a}, Ω_{1b} and Ω_{1c}. Thus, the following 3D results apply the same number of vectors for each subdomain type in the calculations. The 3D error ϵ_{3D} for Case 1 reconstructed by its own modes is shown in Figure 17. 5 and 20 modes are used in the figure. This global 3D representation is built considering the first decomposition strategy of Figure 4. Retaining five modes, the error is about 0.2% in most parts of the bundle. The inaccuracy reduces below 0.1% when 20 modes are utilized.

For the fifth case –blockage–, the 3D error is displayed in Figure 18. Results reveal that the maximum inaccuracies appear in the region near the blockages. Retaining five modes, dissimilarities in the inlet and the blockages-neighboring region are higher than 5%. An accurate representation of velocity in the inlet requires utilizing 20 modes. The results indicate that five modes can well represent the velocity field for an unblocked case. With jams, the velocity distribution upstream and downstream of the blockages is comparatively more complicated, Figure 10. The velocity modulus is low in that region. Thus, the relative error is higher than 5% even when using 20 modes in low-velocity domains, although this is not significant.

Besides, in both cases, high local error exists in the inlet. Since the dominant modes –the first ones– capture the axial flow in most subdomains and the extensive variations near blockages, extra modes are needed to represent the uniform inlet velocity more accurately.

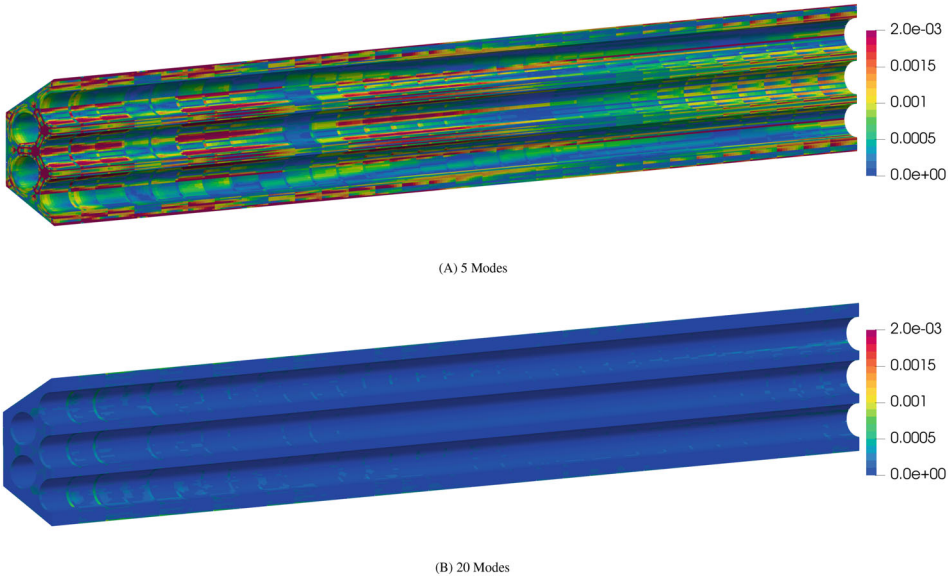

FIGURE 17 3D truncation error ϵ_{3D} of the velocity field for Case 1. The contour is reproduced with (A) 5 and (B) 20 modes in Ω_{1a}, Ω_{1b} and Ω_{1c}.

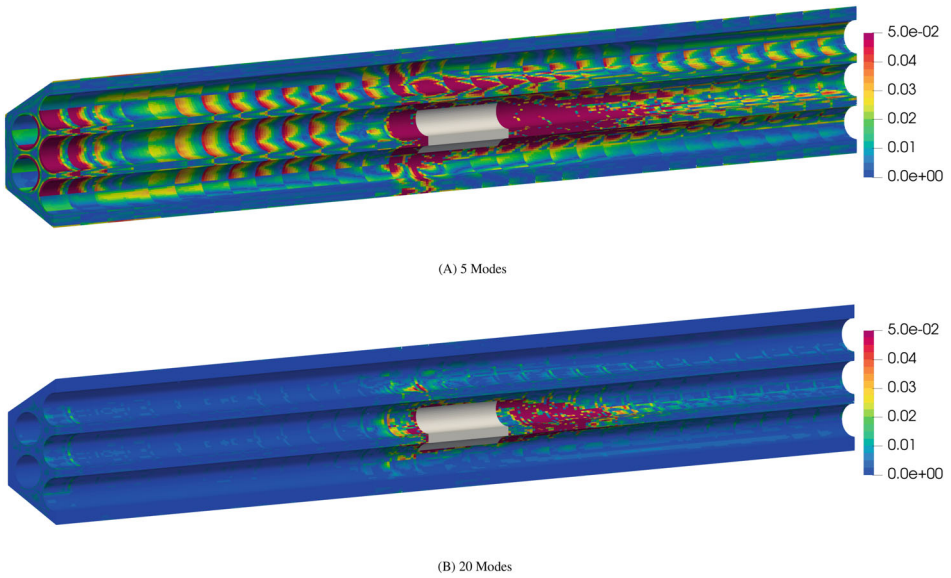

FIGURE 18 3D truncation error ϵ_{3D} of the velocity field for Case 5. The contour is reproduced with (A) 5 and (B) 20 modes in Ω_{1a}, Ω_{1b} and Ω_{1c}.

3.4 | Representative subspace

In the simulations, we have carried out, several distinct physical settings were assumed. This resulted in various particular solutions that nevertheless show some common patterns.

In the local reduced basis technique we are following, we are utilizing a division of the space into subdomains with a relatively small tiling. We utilize the same partitioning in all simulations. Therefore, it is reasonable to expect that a certain –probably high– level of similarity exists among the results obtained locally for some or many of the sub-domains. This similarity should translate into a likeness among the reduced basis arising from each of the individual cases.

In these frames, it is reasonable to study whether the bases arising from a single experiment can supplant all others with acceptable accuracy. This can be claimed utilizing Equation (1). This time the snapshot collection S and the reduced basis Φ, correspond to different cases. We call this *approximation error* and denote it by ϵ_R.

$$\epsilon_R = \frac{\|S_i - \Phi_R \Phi_R^T S_i\|_F}{\|S_i\|_F}, \tag{3}$$

where S_i indicates a snapshot matrix obtained from any case i, and Φ_R is a reduced basis constructed from a so-called representative case. Hence, $i \neq R$ in the following comparisons.

For the rest of this section, we will apply the representative reduced basis Φ_R, obtained from Case 5, to approximate the snapshots of all other calculations. This choice is based on the results in Section 4 and the qualitative estimation for the flow features based on our knowledge and experience. On them, it appears that the subspace obtained from this case seems to be more prone to be able to substitute all others. Besides, the same number of vectors are also utilized to approximate each type of subdomain, denoted Ω_{1a}, Ω_{2a}, Ω_3 and so forth.

Figure 19 displays ϵ_R in subdomains Ω_{1a}. We notice that all curves show a decline. They decrease quickly in the first 20 modes, and then the decay rate slows. For unblocked cases (i.e., Cases 1, 2, and 3), we can observe that the error is less than 1% when using more than ten modes. Then they descend gradually to the order of 1×10^{-4}. For blocked cases (i.e., Cases 4 and 6), the errors are higher than those of previous ones. All errors decrease to 1% after 20 modes. However, the curves of Cases 4 and 6 remain higher than 1×10^{-3} even adopting 100 modes.

It is interesting to study the influence of the domain decomposition strategies proposed in Section 2.2. We plot errors for chosen subdomains for Cases 1 and 4 in Figure 20. In both cases, the errors go down with the increase in the number of modes. Figure 20A shows the results for Case 1. The drop of the curves is rapid within ten modes and then becomes linear. In the whole process, a smaller subdomain usually results in a lower error level. The error for the smallest subdomain, Ω_{1a}, appears to be always the lowest. The last point will be discussed later regarding further results.

For the blocked condition, Case 4, errors are presented in Figure 20B. Notice that the existence of jams leads to a higher approximating deviation than the former results. Remark that the distinctions in Ω_{1a} are much lower than the others. The former remains under 0.5% when using more than 20 modes. However, for the others, the errors amount to 2% at that point. Furthermore, their values decrease more slowly. The curves of Ω_{2a} and Ω_3 require 40 extra modes to underlay under 1%. The error in Ω_4 stays nearly unchanged even if the number of modes increases from 20 to 80. Thus, applying more than 20 modes in Ω_4 to construct ROMs does not yield a significant improvement in accuracy.

As remarked in Section 3.1, the POD basis is the optimized low-dimensional representation of a high-fidelity data set. Approximating a snapshot through a subspace corresponding to another database—the reduced basis of Case 5—introduces an additional discrepancy. Exploring the relations between truncation (on its own reduced basis) ϵ and approximation error (on a reduced basis corresponding to another set) ϵ_R is thus very meaningful. The comparisons of the two are displayed in Figure 21. The figure contains the results in domain Ω_{1a}.

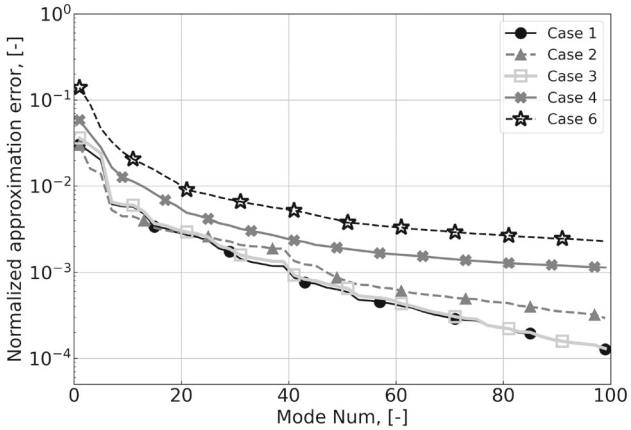

FIGURE 19 Error ϵ_R obtained approximating Cases 1, 2, 3, 4, and 6 based on the representative basis of Case 5. The Effect of physical setups.

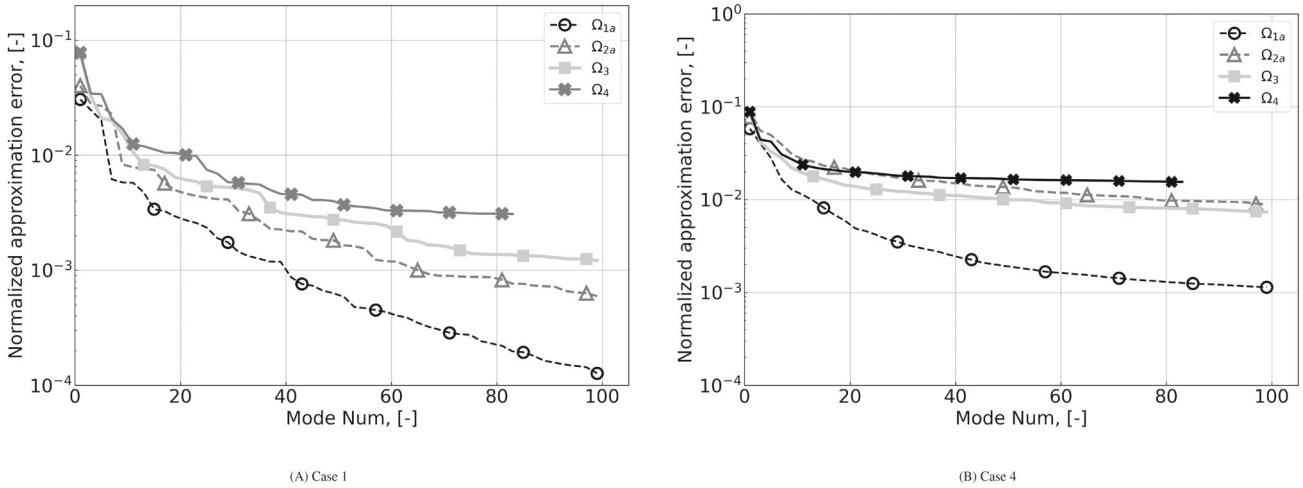

FIGURE 20 Error ϵ_R obtained approximating Cases 1 and 4 based on the representative basis of Case 5. The effect of division shapes.

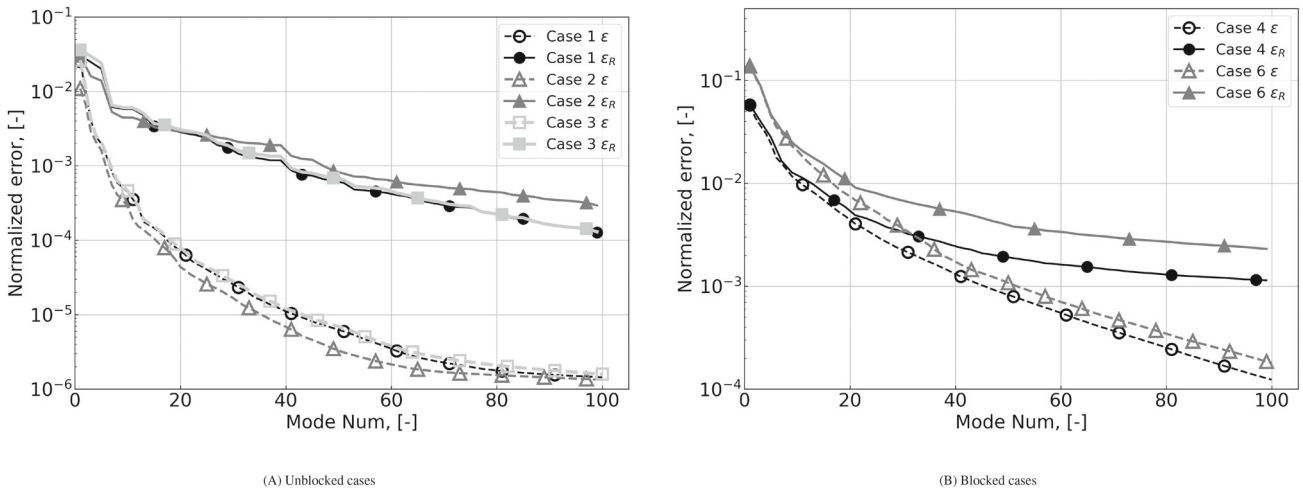

FIGURE 21 Comparison of the inaccuracy utilizing its own reduced basis (truncation error ϵ) and the one of Case 5 (approximation error ϵ_R). Velocity in Ω_{1a} for (A) unblocked (1, 2, and 3) and (B) blocked cases (4 and 6).

Figure 21A shows the notable difference between the two errors for unblocked situations. The gap between the curves enlarges with the mode number. Notice that at the point of 20th mode, ϵ underlies 1×10^{-4}, while ϵ_R remains at 2×10^{-2}.

The comparisons between Cases 4 and 6 are shown in Figure 21B. The distinctions between the two errors are narrow regarding the previous comparisons. Within the first 20 modes, they are comparable. In contrast, the difference cannot be neglected after 40 modes. Considering the flow complexities induced by the flow obstruction, we necessitate more reduced basis vectors to approximate the high-fidelity solutions with acceptable accuracy.

Previous quantities based on the Frobenius norm consider overall results. We now analyze the 3D distribution of the approximation error, which can be computed similarly to Equation (2). In the following results, an identical number of vectors were adopted to compute the ϵ_R of all divisions of each shape.

Figure 22 shows the 3D error for Case 1. The values are computed adopting 20 velocity modes in subdomains Ω_{1a}, Ω_{1b} and Ω_{1c}. Remark that the velocity in blockage-neighboring regions might be close to zero, so the 3D relative errors are weighted with a small value to eliminate the extremely huge local errors. The weight factor is appropriately selected as 1% of the maximum velocity. The local error stays around 1% in the whole bundle. However, the inner subchannels are not well approximated. Recall that blockages are located in inner subchannels. Thus, dominant modes capture the flow pattern near the obstruction. Notice that the maximum magnitude appears in the inlet, indicating that flow features of uniform inflow are not well captured.

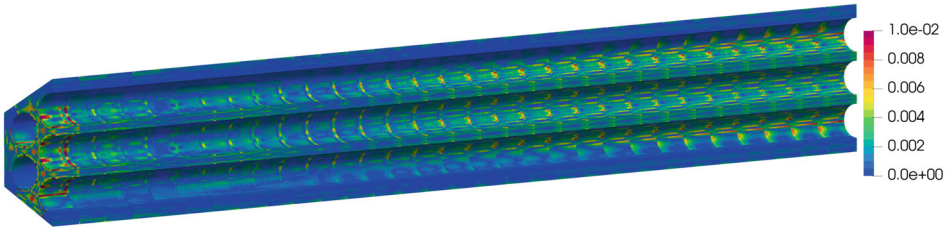

FIGURE 22 3D approximation error of the velocity for Case 1. The contour is reconstructed by using 20 vectors of Φ_R in Ω_{1a}, Ω_{1b} and Ω_{1c}.

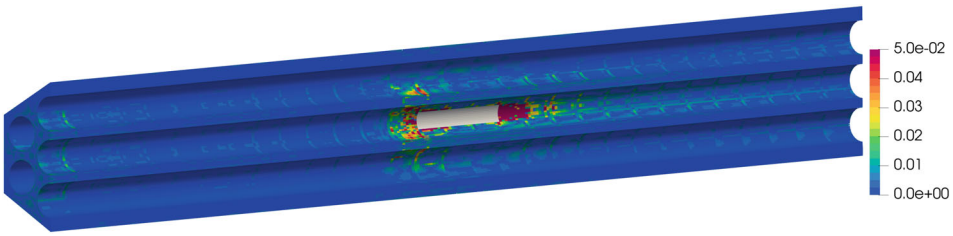

FIGURE 23 3D approximation error of the velocity for Case 4. The contour is reconstructed by 20 modes of Φ_R in Ω_{1a}, Ω_{1b} and Ω_{1c}.

The 3D plot for Case 4 is shown in Figure 23. We see that the error remains under 5% in most locations except near the blockages. As displayed in Figure 18, the maximum also appeared around the blocking regions.

4 | DISTANCES BETWEEN LINEAR SUBSPACES

Due to the geometric particularities of the bundle –symmetries, pitch, and so forth–, it is conceivable that the principal components of the flow in some or many subdomains have some degree of similarity. We intend now to characterize this by analyzing the distances between them.

4.1 | Introduction and definition

The definition of distances among high dimensional linear subspaces is not trivial.[72] It is carried out in frames of a compact smooth manifold called Grassmannian, $\mathrm{Gr}(k, n)$. This construction parameterizes all k-dimensional linear subspaces of a n-dimensional vector space.

We consider at this stage the solutions of two simulations that we name A, B. By *simulation,* we denote a collection of solutions sampled, for example, at different times, and arranged in matrix form. We defined the fields in vector form as a_i and b_i, with i being any of the times involved. Certainly, $A = (a_1, a_2, \dots, a_n)$ and $B = (b_1, b_2, \dots, b_n)$. We obtain a reduced basis for each of them by applying the singular value decomposition procedure. Those are $X = (x_1, x_2, \dots, x_m)$, $Y = (y_1, y_2, \dots, y_m)$, where x_i and y_i are the ortho-normal vectors of the reduced basis. Let us define $\hat{X} = \mathrm{span}(x_1, x_2, \dots, x_k)$ and $\hat{Y} = \mathrm{span}(y_1, y_2, \dots, y_k)$. The distance we are interested in is $d(\hat{X}, \hat{Y})$. To simplify the notation, we drop circumflex accents and denote the subspace and the matrix containing its basis vectors, implicitly identifying both concepts.

For the subspaces $X, Y \in \mathrm{Gr}(k, n)$, we create a matrix $X^{\mathsf{T}}Y$, and apply the singular value decomposition algorithm to it. We get

$$X^{\mathsf{T}}Y = L\Sigma R^{\mathsf{T}}, \tag{4}$$

where $\Sigma = \mathrm{diag}(\sigma_1, \dots, \sigma_k)$ are the singular values, fulfilling $1 \geq \sigma_1 \geq \cdots \geq \sigma_k \geq 0$.

TABLE 3 Distances defined on $\mathrm{Gr}(k,n)$ in terms of principal angles and orthonormal bases.[54]

No.	Distance	Principal angles	Orthonormal bases	Range
1	Grassmann	$d_{\mathrm{Gr}(k,n)}(X,Y) = \left(\sum_{i=1}^{k}\theta_i^2\right)^{1/2}$	$\|\cos^{-1}\sum\|_F$	$[0, k\pi/2]$
2	Asimov	$d^{\alpha}_{\mathrm{Gr}(k,n)}(X,Y) = \theta_k$	$\cos^{-1}\|X^{\mathsf{T}}Y\|_2$	$[0, \pi/2]$
3	Chordal	$d^{\kappa}_{\mathrm{Gr}(k,n)}(X,Y) = \left(\sum_{i=1}^{k}\sin^2\theta_i\right)^{1/2}$	$\frac{1}{\sqrt{2}}\|XX^{\mathsf{T}} - YY^{\mathsf{T}}\|_F$	$[0, \sqrt{k}]$
4	Projection	$d^{\pi}_{\mathrm{Gr}(k,n)}(X,Y) = \sin\theta_k$	$\|XX^{\mathsf{T}} - YY^{\mathsf{T}}\|_2$	$[0, 1]$
5	Procrustes	$d^{\rho}_{\mathrm{Gr}(k,n)}(X,Y) = 2\left(\sum_{i=1}^{k}\sin^2(\theta_i/2)\right)^{1/2}$	$\|XL - YR\|_F$	$[0, \sqrt{2k}]$
6	Spectral	$d^{\sigma}_{\mathrm{Gr}(k,n)}(X,Y) = 2\sin(\theta_k/2)$	$\|XL - YR\|_2$	$[0, \sqrt{2}]$
7	Binet–Cauchy	$d^{\beta}_{\mathrm{Gr}(k,n)}(X,Y) = \left(1 - \prod_{i=1}^{k}\cos^2\theta_i\right)^{1/2}$	$(1 - (\det X^{\mathsf{T}}Y)^2)^{1/2}$	$[0, 1]$
8	Fubini–Study	$d^{\phi}_{\mathrm{Gr}(k,n)}(X,Y) = \cos^{-1}\left(\prod_{i=1}^{k}\cos\theta_i\right)$	$\cos^{-1}\lvert\det X^{\mathsf{T}}Y\rvert$	$[0, \pi/2]$
9	Martin	$d^{\mu}_{\mathrm{Gr}(k,n)}(X,Y) = \left(\log\prod_{i=1}^{k}1/\cos^2\theta_i\right)^{1/2}$	$(-2\log\det X^{\mathsf{T}}Y)^{1/2}$	$[0, +\infty)$

We now introduce a fundamental concept, that of the *principal angle*. The principal angles $\theta_1 \leq \cdots \leq \theta_k$ between the two subspaces are formulated as

$$\theta_i = \cos^{-1}\sigma_i, \quad i = 1, \ldots, k. \tag{5}$$

Each of them is formed among the rays defined by pairs of principal vectors (f_i, g_i), which can be computed as,

$$[f_1, \ldots, f_k] = XL, \quad [g_1, \ldots, g_k] = YR. \tag{6}$$

Note that principal angles play a notable role in the theory of distances among linear subspaces. Remark that it has been proven that any definition of distance must be done as a function of principal angles.[54] Various widely accepted distances between linear subspaces are listed in Table 3.[53,54]

4.2 | Interpretation

Even if the definitions of distances in the table seem complicated at first glance, they have precise physical meanings. In the paragraphs below, we will attempt its clarification.

As shown above, each of the i principal angles represents the dissimilarities among the corresponding pair of principal vectors. The principal angles can be arranged in a vector $(\theta_1, \ldots, \theta_k)$, whose module can be characterized by different norms. In those terms, **Grassmann** distance corresponds to the Euclidean norm and **Asimov's** to the uniform of that vector containing the principal angles. We may also see the principal angles as the sides of a k-dimensional parallelogram, in which the **Grassmann** distance corresponds to the sum of the diagonals of that parallelogram.

The inconsistency between two subspaces can be indicated in several ways, that is, by studying the dissimilarities in all or the worst direction. Note that this ideological difference not only links Grassmann and Asimov distances, but will also connect Projection-Chordal and Spectral-Procrustes distances. Remark that when two subspaces almost overlap but are very distinct in one dimension, considering just the largest component might emphasize dissimilarities, failing to represent the real closeness among them.

Let us recall now that the projection matrix on an X subspace is given by $P = XX^{\mathsf{T}}$. In these terms, distances three and four are the norm of the difference between the projectors of the two subspaces. **Chordal** distance utilizes the Frobenius norm, which is the Euclidean norm relating to all singular values of the difference matrix. **Projection** distance –2-norm– only considers the largest singular value. Regarding angles, the **Chordal** formula can be interpreted as the Euclidean norm of the areas of the parallelograms created by each pair of principal vectors. The **Projection** form only evaluates the maximum one.[†]

Following Equation (6), the matrices XL, YR contain the principal vectors by columns. **Procrustes** distance can be regarded as the Euclidean norm of singular values of the metric matrix among principal vectors, while **Spectral** distance uses only the maximum singular value. In terms of angles, **Spectral** can be reformulated as $\sqrt{2}\sqrt{1-\cos\theta_k}$. Since the

principal vectors are normalized, $\cos\theta_k$ is regarded as the inner product of the less aligned pair, (g_k, f_k). Therefore, $1 - \cos\theta_k$ denotes the deficit due to this misalignment. **Procrustes** adopts the Euclidean norm of the misalignment for each pair of principal vectors.

The determinant of a matrix gives the signed volume of the parallelotope generated by the vectors given by its columns.[73] An identity matrix may be interpreted as a k-dimensional hypercube that has a volume -determinant- of 1. Therefore, $det(X^{\mathsf{T}}Y)$ gives the volume of a k-dimensional parallelotope generated by the linear transformation $X^{\mathsf{T}}Y$. If the two orthogonal matrices are the same, then $X^{\mathsf{T}}Y$ leads to an identity matrix, and the volume of the parallelotope is 1. When two subspaces become less similar, the parallelotope is distorted, resulting in a smaller volume.

Binet–Cauchy distance corresponds to this volume deficit. Alternatively, we can give an interpretation in terms of principal angles. The misalignment between vectors forming the parallelotope generated by $X^{\mathsf{T}}Y$ can be characterized by their inner product. Since all vectors involved are normalized, the inner product is itself specified by their cosines.

Note that the volume is bounded by zero and one, so it can be converted into an angle via *arccosine*. This is the definition of the **Fubini–Study** formula in terms of orthonormal bases.

Finally, we remark that the log-determinant function can be interpreted as the unit ellipsoid generated by the linear transformation $X^{\mathsf{T}}Y$, $x^T X^T Y x \leq 1$. Its volume is proportional to the square root of the product eigenvalues of $X^{\mathsf{T}}Y$. Note that the matrix is a shrinking linear transformation. This fact allows us to define the **Martin** distance as a measure of this volume reduction.

4.3 | Gathered snapshots

As a first study, we collected the snapshots of all six cases into a common data set. The reduced basis was obtained by POD and represents the dominant flow patterns in all cases. Note that the common patterns are the dominant as a whole and should not forcefully include all dominant modes –up to an accuracy threshold– of each case. With this study, we intend to analyze whether a single common basis can accurately reconstruct the flow patterns in all cases. The patterns not included can be actually interpreted as the distance between the individual and the common basis.

Remark that the importance of lower modes is more significant than higher ones. Above a certain number, vectors are just due to the numerical noise that exists in the solutions, for which comparisons are irrelevant. Therefore, to exclude this impact, in the subsequent paragraphs, we only compare the first 20 and 40 vectors for unblocked and blocked cases, respectively.

4.3.1 | Basic comparisons of all distances

Distances between the subspace generated by the gathered reduced basis and those corresponding to Cases 1 and 5 are displayed in Figure 24 for domain Ω_{1a}. Remark that the subspaces contain an equal number of vectors in the calculations.

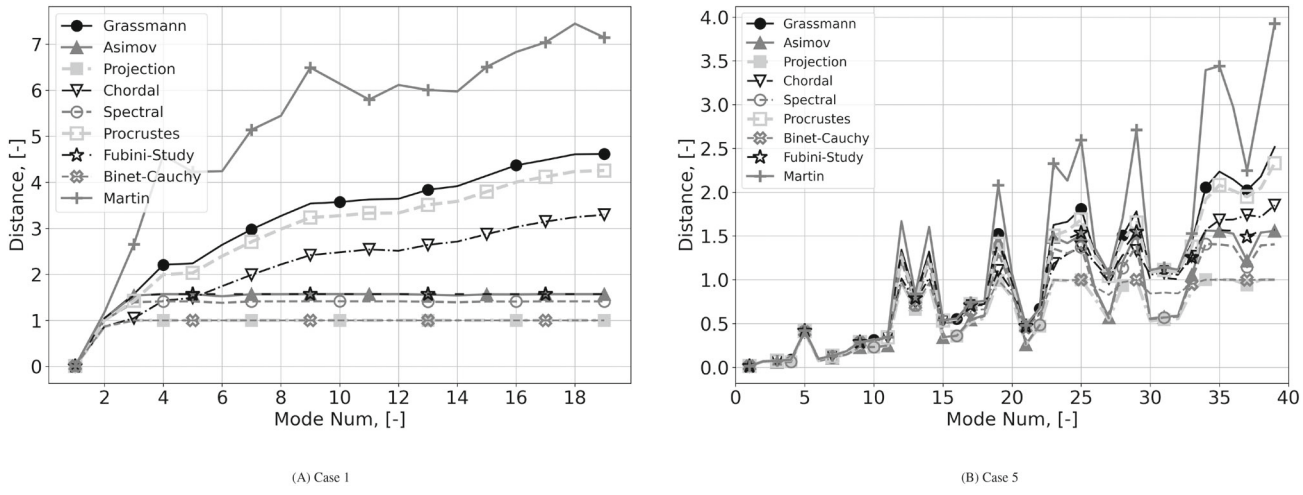

FIGURE 24 Subspace distance between velocity modes of gathered and Cases 1 and 5 in Ω_{1a}.

The results in Figure 24A reveal that the dominant modes of Case 1 and the ones of the gathered database are very dissimilar. The results corresponding to Case 5 are displayed in Figure 24B. They also show an upward trend but a smaller slope compared to the one in Case 1. Thus, the common database is dominated by cases with blockages.

Of particular interest in understanding the dissimilarities among subspaces are the smaller principal angles. For a ROM, they correspond to basis vectors that will probably be the ones with larger amplitudes. They also contain the most significant flow patterns.

In Case 1 Figure 24A, the agreement between the lower modes of the gathered and own subspaces is relatively poor. Note that Asimov, Projection, Spectral, and Binet-Cauchy distances reach their upper bounds in less than five modes, while that happens in Case 5 only after twenty modes. The Grassmann, Chordal, and Procrustes distances grow in a similar way. According to the definitions of distances, the last ones consider the effect of all principal angles, while Asimov, Projection, and Spectral only consider the maximum one. Therefore, this result indicates that as early as the fifth mode, the subspaces are orthogonal in one dimension for Case 1. But even if the agreement is better with Case 5, the angle is as large as $\pi/4$ for the 15th mode. Note also the relatively low importance of the first angles for calculating the distance, despite its importance for the ROM. Computing distances with several modes, the larger –last– principal angle is dictating the trend compared to the others.

Regarding the Binet-Cauchy distance, we observe that for Case 1, it reaches its maximum after five modes. This indicates that the linear transformation by the matrix $X^{\mathsf{T}}Y$ has converted the parallelotope into a body of at least a dimension less.

Finally, the Martin distance increases with a larger trend than the others. This means that in both cases, the transformation of the matrix is far from an ideal sphere, becoming a significantly deformed ellipsoid.

Observe that the above comparison illustrates that all distances vary similarly until reaching their upper bound.

4.3.2 | Effect of blocked and unblocked conditions

In the previous figures, we just present results subjected to Cases 1 and 5. We will show that these two suffice to represent the blocked and unblocked scenarios. To do it, we now repeat the comparisons under the same conditions as before. For the clarity of the discussion, we restrict ourselves to two distances, that of Grassmann and Fubini–Study. The selection does not reduce the pertinence of the description since the two metrics can represent the two typical trends shown in Figure 24.

In Figures 25 and 26, we confirm that the distance of unblocked conditions is much higher than that of blocked ones. The dominant flow modes without blockages correspond to axial flow. In contrast, the flow behavior near the jams has a transversal component, resulting in a more complex pattern. The gathered dominant modes are built to capture the latter. This results in smaller distances to blocked cases.

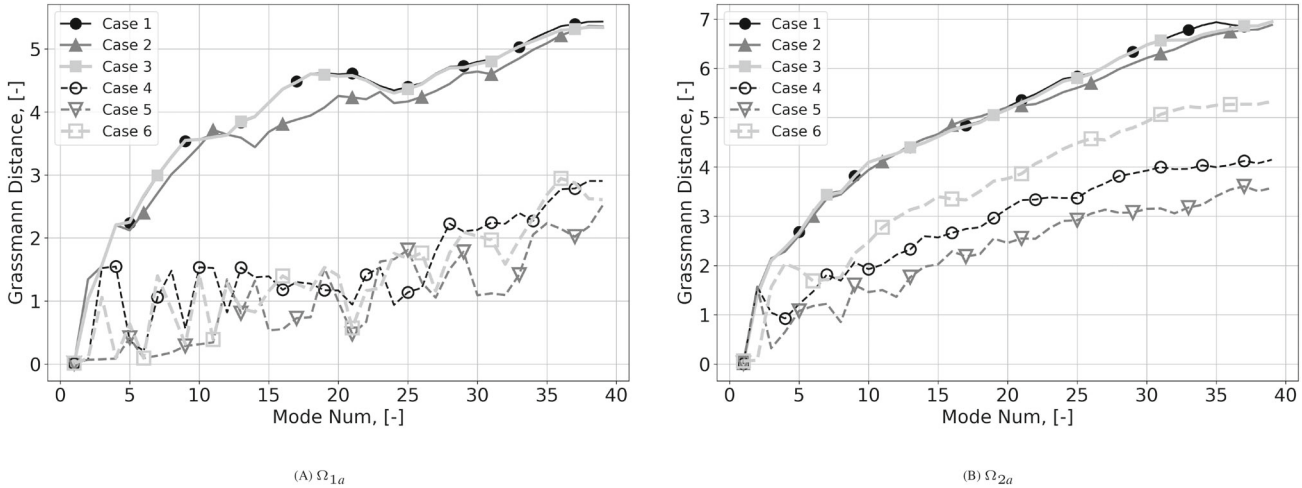

FIGURE 25 Grassmann distance between velocity modes of gathered and cases in Ω_{1a} and Ω_{2a}.

In both comparisons –following the trend of Figure 25–, the distance related to Case 5 is the smallest, indicating that the dominant features are more similar to that case than the others. Besides, we also remark that distances are smaller in the subdomain Ω_{1a}. Thus, the snapshots can be better approximated using the domain decomposition strategy regarding smaller subdomains.

The curves displayed in Figure 26 show a different trend compared to the previous results. For Fubini distance, all lines fastly reach a maximum for sufficiently high N. As discussed beforehand, the Fubini–Study gives the value of the arccosine of the volume of a transformed n-dimensional parallelotope. If there exists an extensive rotation in one dimension, the parallelotope is significantly compressed after the linear transformation $X^{\mathsf{T}}Y$ and leads to a minimal volume. That is why the upper bound $\pi/2$ for the Fubini–Study is rapidly obtained.

This peak can be explained regarding the reduced basis of the gathered case, mainly accounting for the flow distortions induced by blockages. In Ω_{2a}, Cases 1, 2, and 3 reach the peak in less than five modes. Such variation is also observed in Ω_{1a}. Contrarily, the results of Cases 4, 5, and 6 arrive the highest after 35 modes (in Figure 26A).

4.3.3 | Effect of the subdomains

To gain further knowledge about the effect of domain decomposition strategies, the Grassmann and Fubini distances of different divisions are compared in Figures 27 and 28.

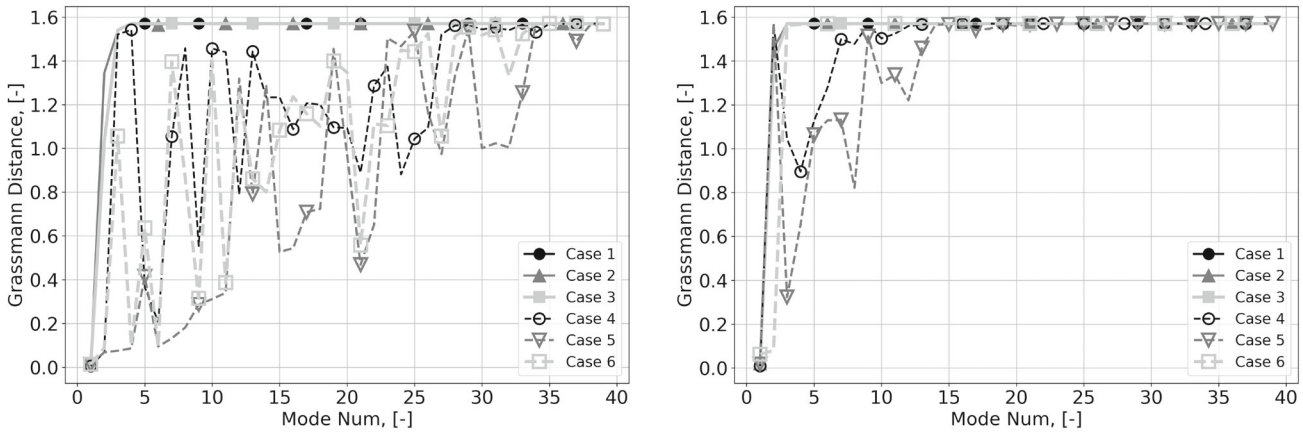

FIGURE 26 Fubini–Study distance between velocity modes of gathered and cases in Ω_{1a} and Ω_{2a}.

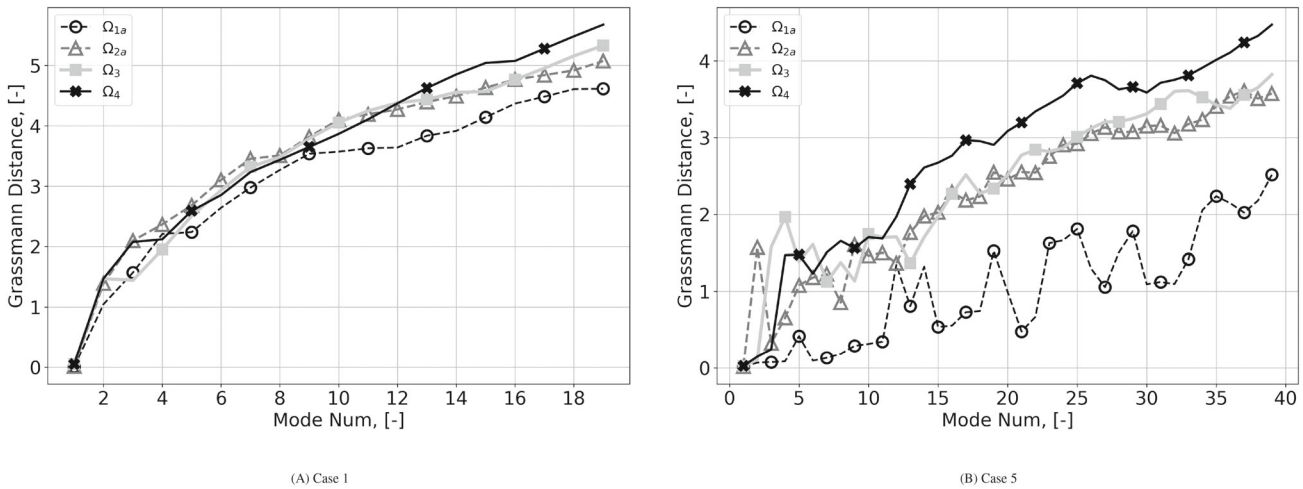

FIGURE 27 Grassmann distance for velocity modes in Ω_{1a}, Ω_{2a}, Ω_3, and Ω_4 between gathered and Cases 1 and 5.

As shown in Figure 27, we observe that a reduced subdomain size generally results in smaller distances, and the difference increases with the mode number. Distances in Ω_{1a} are smaller than in the others. Although the size of Ω_{2a} is smaller than Ω_3, the distances among them are relatively small. Remark that the blockages are located exclusively in inner subchannels. Therefore, flow patterns are simpler in edge and corner zones. The flow complexity is restricted to domain Ω_{2a}, while parts Ω_{2b} and Ω_{2c} remain quite simple. Hence, it is slightly advantageous to follow a division strategy with more partitions, the one of strategy 2. In strategy 4, the complexity touches the whole enlarged domain.

Tendencies are exacerbated by Fubini distance in Figure 28. For Case 1, all lines reach the highest point after only five modes. Without the extra flow features near the blocking regions, Case 1 is far away from the gathered snapshots. For Case 5, the Fubini–Study distance gives a similar trend as Grassmann.

4.4 | Separated comparison of blocked and unblocked cases

Results in Section 4.3 indicate that the reduced basis of blocked and unblocked cases behave distinctively. Thus, the distances among these cases are now analyzed separately. Grassmann and Fubini–Study distances for cases with and without blockages are shown in Figures 29 and 30, respectively. The figures display the comparisons of velocity modes in subdomain Ω_{1a}.

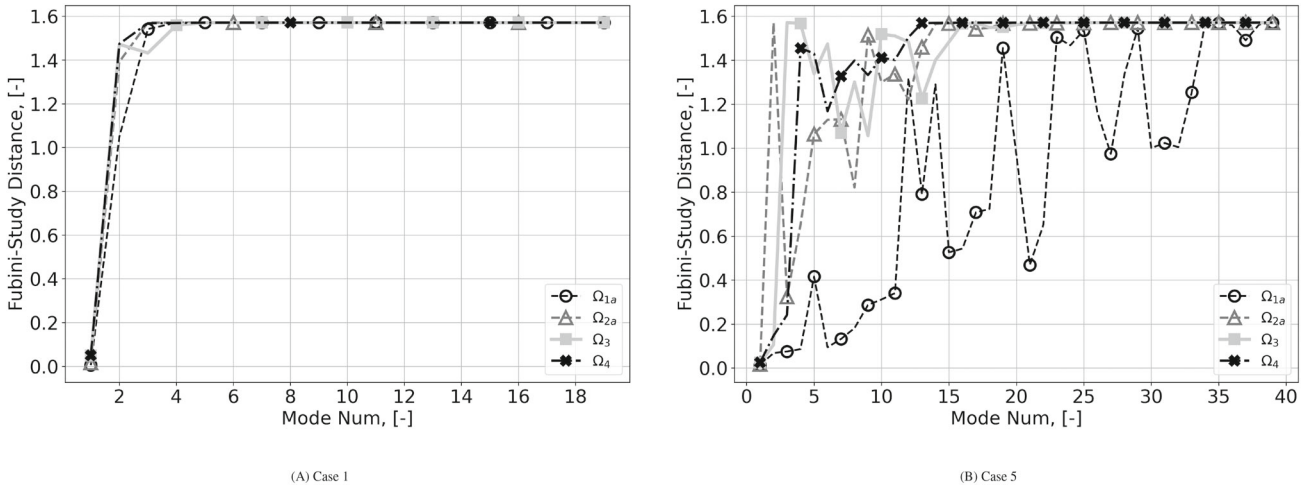

FIGURE 28 Fubini–Study distance for velocity modes in Ω_{1a}, Ω_{2a}, Ω_3, and Ω_4 between gathered and Cases 1 and 5.

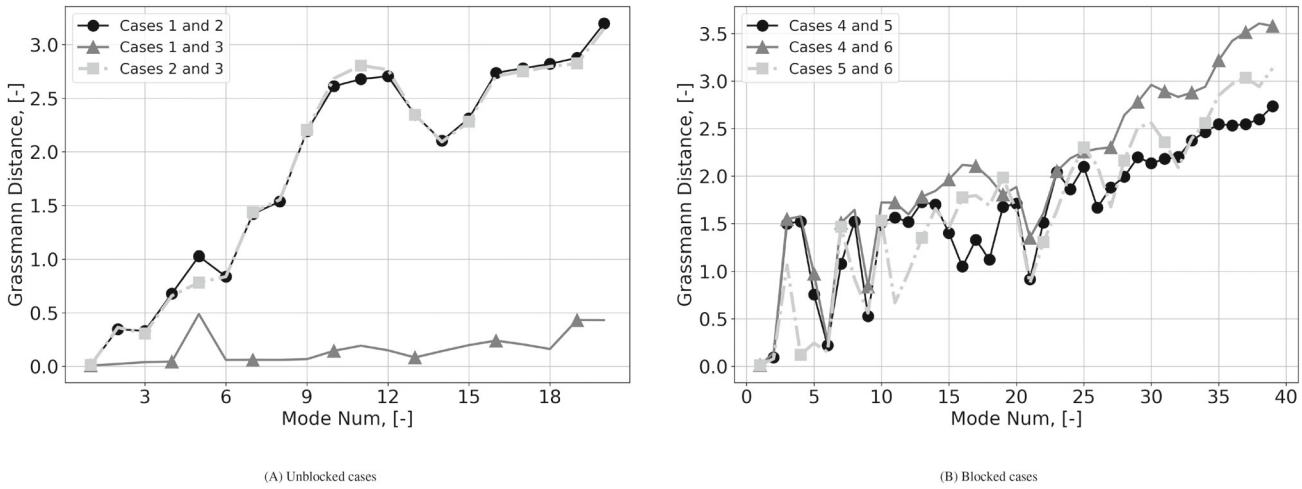

FIGURE 29 Grassmann distance among velocity modes in Ω_{1a} of unblocked cases (i.e., Cases 1, 2, and 3) and blocked cases (i.e., Cases 4, 5, and 6).

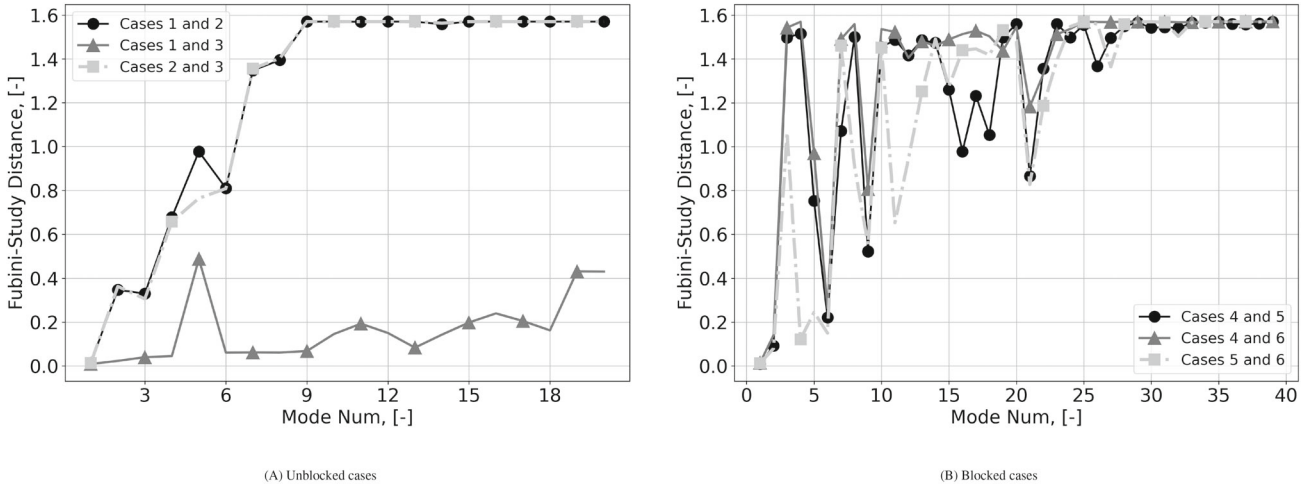

FIGURE 30 Fubini–Study distance among velocity modes in Ω_{1a} of unblocked cases (i.e., Cases 1, 2, and 3) and blocked cases (i.e., Cases 4, 5, and 6).

For the no-obstructions cases of Figure 29A, we see that the Grassmann method gives a relatively low distance between Cases 1 and 3, which is within $\pi/6$ even when the mode number is increased to 20. This is also confirmed by the Fubini–Study approach in Figure 30A. Remark that Cases 1 and 3 differ only in the inflow velocity. That accounts for the distances appearing in the figure.

An important feature of the plots is the peak of $\pi/6$ we can observe in the fifth mode. Then the distance decreases again after it. That corresponds to a situation in which the bases for the two cases are very similar but with two vectors swapped. Note that from the POD procedure, the ordering of the vectors corresponds to their relative importance in the collection of snapshots. Due to the swapping and adding an extra coordinate into the two subspaces, the distinction is greatly diminished.

Considering the relations between Cases 2 to 1 and 3 (in Figure 29A), the Grassmann distance rises gradually, indicating the growing dissimilarities among them. Nevertheless, there are valleys for both curves in mode 14. That effect is also caused by the sequential exchange of modes, as mentioned above.

The Fubini–Study distance, see Figure 30A, presents a maximum value of $\pi/2$ after nine modes. The increased value compared to that of Cases 1 and 3 is due to the flow distribution at the inflow. Case 2 is fully developed, hence their modes cannot capture flow patterns regarding the developing process of the flow as in 1 and 3.

The results of Grassmann distance for blocked cases are displayed in Figure 29B. Here, the discrepancy among the three conditions increases even when a few modes are considered. The level of $\pi/2$ is reached already with three dimensions. The lines fluctuate around this value for the following 20 modes. This pattern can be confirmed in Figure 30B. The values of $\pi/2$ for a few modes, as shown in Figure 30B, are related to some particular perpendicular vectors. Increasing the number of modes, the distances decrease dramatically and then jump again. This implies that similar flow patterns are of different but close importance for the three cases. Therefore, for the first 25 modes, the global content –not its relative importance– is comparable. The peaks do not occur in the same locations for the three comparisons (e.g., Cases 4 and 5 around mode 18). The influence of the blockage ratio in the flow features is significant.

From the above comparisons, we conclude that the change in inlet velocity results in relatively low distances for unblocked conditions. The existence of blockages significantly impacts the corresponding reduced subspaces, leading to a few perpendicular vectors between the subspaces.

As a general conclusion on the relative usability of the distances, the results indicate that the Fubini–Study, Asimov, Projection, Spectral, and Binet-Cauchi distances show better performance in measuring very close subspaces, while Grassmann, Chordal, Procrustes, and Martin can better capture conditions that are more dissimilar.

4.5 | Distances among subspaces of different dimensions

4.5.1 | General definitions

The methodology to calculate distances between subspaces of non-equal dimensions is described in detail by Ye et al. in Reference 54. Here we just provide minimal information for completion.

Assume we have two subspaces $X \in \mathrm{Gr}(k,n)$ and $Y \in \mathrm{Gr}(l,n)$, and let $k \leq l \leq n$. We define two subsets

$$\Omega_+(X) := \{E \in \mathrm{Gr}(l,n) : X \subseteq E\},$$
$$\Omega_-(Y) := \{F \in \mathrm{Gr}(k,n) : F \subseteq Y\},$$

where $\Omega_+(X)$ contains all *extensions* of X into a subspace of l dimension, and $\Omega_-(Y)$ represents the set of all *restrictions* of Y into k.

Two definitions of the distances between X and Y can be formulated in terms of the restriction $\delta_1(X, \Omega_-(Y))$ and the extensions $\delta_2(\Omega_+(X), Y)$. They are formulated as

$$\delta_1(X, \Omega_-(Y)) = \min_{F \in \Omega_-(Y)} \delta(X, F), \tag{7}$$

and

$$\delta_2(\Omega_+(X), Y) = \min_{E \in \Omega_+(X)} \delta(E, Y). \tag{8}$$

The two formulations are equal,[54] $\delta_1(X, \Omega_-(Y)) = \delta_2(\Omega_+(X), Y) = \delta(X, Y)$.

As in Section 4.1, we may formulate the distance in terms of principal angles. That can be computed by Equation (4). Then, the Grassmann distance is given by

$$\delta(X, Y) = d_{\mathrm{Gr}(k,n)}(X, \Omega_-(Y)) = \left(\sum_{i=1}^{k} \theta_i(X, Y)^2 \right)^{1/2}. \tag{9}$$

Similarly, the other definitions of distances in Table 3 in terms of principal angles can be utilized.

4.5.2 | Comparison among individual and gathered subspaces

We start now analyzing if individual subspaces can be included in the gathered one, provided the latter is much larger.

The reduced basis of gathered snapshots contains flow features of all cases, with and without blockages. Since a case can only be optimally approximated by its own reduced basis, one should use more dimensions of the gathered basis for the same accuracy. Therefore, we compute distances between each individual subspace and the gathered one. In the comparison, we take a relatively low dimension for each individual subspace and vary the one of the gathered. Note that the distance denotes the amount of individual flow information not involved in the gathered subspace.

Note that the Grassmann and Fubini–Study metrics are extensively used in the above analysis. Thus, to better understand the properties of the other distances, Martin and Projection approaches are utilized for comparisons in the subsection. The results applying the two approaches are plotted in Figure 31 where velocity modes in the domain Ω_{2a} are compared. We select ten modes for each individual case while varying the dimension of the gathered basis in the range of 10 to 40.

Results of Figure 31A indicate that the Martin distances of unblocked cases decrease linearly, that is, slowly. The lines of Cases 1 and 3 almost overlap. This is because their modes are very similar. Case 2 has a lower trend, revealing that, in this case, its subspace is closer to the gathered basis. That was not detected in the previous comparisons.

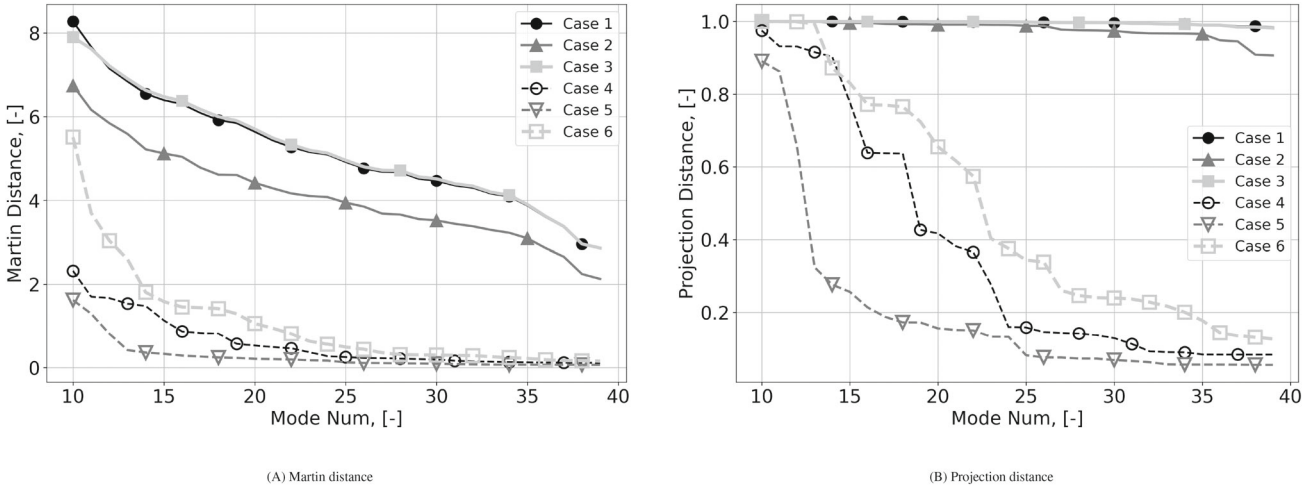

(A) Martin distance

(B) Projection distance

FIGURE 31 Martin and projection distance between the different number of velocity modes of gathered (x-axis) and cases (10 modes) in Ω_{2a}.

The distances of obstructed cases to the common subspace are smaller than previous ones. The three results quickly decline when increasing the x-axis from 10 to 15. The curves are smaller than $\pi/2$ after 20 modes and stay at a relatively low value. We can see that the distance of Case 5 is the lowest in the whole range.

The Projection distances are displayed in Figure 31B. Observe that the distance of non-jammed cases is nearly one. Thus, at least one perpendicular principal vector exists between the two bases.

For blocked cases, the distances continuously decrease. The value is lower than one when employing 15 gathered modes. So there are normal vectors at that point. Even considering the maximum principal angles, all lines are less than 0.4 after 25 modes. That reveals the flow features caused by blockages are well captured –and dominant– in gathered modes.

4.5.3 | Independent comparison between blocked and non-blocked cases

We confirmed that unblocked and blocked cases contain different flow patterns. Therefore, we compare the distances among them separately.

Figure 32 represents the Projection distances of cases without obstacles. In the diagram, the velocity modes in subdomain Ω_{2a} are shown. The dimension of Cases 2 and 3 is kept constant to five. The modes of Case 1 are increased from 5 to 20.

We notice that the distance between Cases 1 and 2 decreases by adding the sixth mode. Then it remains around 0.8 even if we use 20 modes. We can thus state that a certain proportion of flow characteristics in Case 2 cannot be represented by the modes of Case 1.

The result for Cases 1 and 3 remains at one until the ninth mode is included. Then it remains very low in the rest of the scope. That emphasizes that the content of the two bases is almost the same, but the modes appear in a different order. The reduced subspace of Case 3 can include that of Case 1, and vice-versa, provided enough additional modes are included.

Results for the blocked cases shown in Figure 33 illustrate the Projection distance among them. We keep the dimensions of Cases 4 and 6 constant and equal to ten and set the range of variation for Case 5 from 10 to 40. More modes are required to capture the flow complexities of blocked regions. Hence, we use ten basis vectors instead of five as a basic case here.

Notice that the two results decrease gradually. But the value is higher than 0.75 even with 30 modes. Considering the diversity in blocking, there are some dissimilarities between the jammed cases. Thus we cannot get a relatively low value as in Figure 32. However, in the comparisons of 4 and 5 with a maximum principal angle remaining under one, there are no normal directions, and a larger similarity between the subspaces can be obtained by increasing the dimension of the basis.

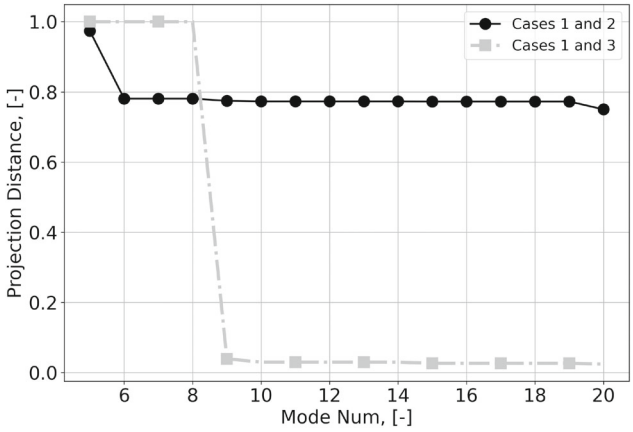

FIGURE 32 Projection distance between the different number of velocity modes of unblocked cases in Ω_{2a}. Case 1 (x-axis); Cases 2 and 3 (5 modes).

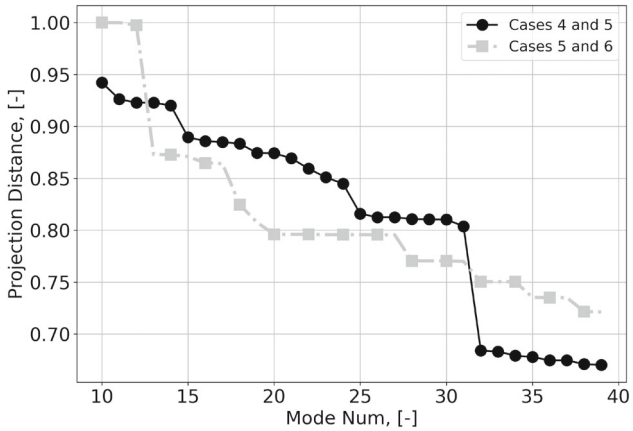

FIGURE 33 Projection distance between the different number of velocity modes of blocked cases in Ω_{2a}. Case 5 (x-axis); Cases 4 and 6 (10 modes).

The comparison of Cases 5 and 6 shows a different trend. The line starts at a value close to one, denoting the existence of at least one orthogonal dimension among them. Then, a sharp descent can be observed at the 13th mode. We may explain this decrease in view of flow patterns. Vectors contain some features that are relevant to Case 6. A similar behavior also exists in the comparison of Cases 4 and 5. The descent is also found, here in its 32nd mode.

5 | CONCLUSIONS

In this research, we have intentionally focused on the first stage of the creation of a reduced model: the construction of a linear reduced subspace. The selection of a local method, four domain decomposition strategies, and six calculations considering different factors increase the complexity of the problem. Those should be studied and, if possible, optimized. In particular, we regard: (a) the determination of appropriate geometrical divisions; (b) the possibility of the creation of a sub-optimal but common subspace for all calculations; and (c) the quantification of the differences among the various options.

To address such issues, in the context of our applied research, we have performed a series of high-fidelity simulations for a 7-pin nuclear fuel bundle, employing an in-compressible OpenFOAM solver. We have applied this to a severe accident relevant to the nuclear industry. The geometry contains a high degree of symmetry and a repetitive disposition. Calculations address several physical scenarios, including instances containing flow blockage, a condition highly

pertinent to this study. Four domain decomposition strategies are utilized to collect the information. Optimal bases are extracted with POD for the ulterior analysis.

A first analysis of the potential accuracy achievable with a reduced basis may be derived by assessing the truncation error. This magnitude describes the errors among fields and their reduced equivalent reconstructions utilizing the POD basis. We can conclude that no matter which subdomains are adopted, all cases can be well represented by subspaces derived from their own snapshot collection (individual subspaces).

A representative subspaces, generated from Case 5, were also applied to reconstruct the other cases. This constituted an attempt to consistently approximate all patterns based on a unique calculation. The procedure can produce acceptable reconstructions for conditions without obstructions. However, the approach is challenged due to the flow complexities around the obstacles. The variations of the previous two approximations emphasize the limitations of using an external reduced basis.

Regarding the tilling of the space, we have concluded that we can generally obtain more accurate representations utilizing small subdomains.

The results indicate dissimilarities among the different calculations. Those naturally translate into differing reduced subspaces. The distances between these linear subspaces are employed as a quantitative measure.

In these terms, we observed that the subspace created on snapshots gathered from all cases (gathered-subspace) shows dissimilarities with each subspace obtained from individual collections. The metrics are distinct for the three blocked scenarios but are relatively close for the three unblocked ones.

Based on this behavior, cases could be separated into two distinct groups depending on whether they are obstructed or not. This division emphasizes the remarkable difference in reduced basis vectors due to physical configurations.

Significant fluctuations were observed in the distances among subspaces. Those depend on the number of dimensions of the reduced basis and vary wildly. We have concluded that they are due to flow patterns that have similar features but are differently ordered in different cases. Therefore, we infer that significant potential benefits can be gained by considering vectors of similar importance in packs. Adding or removing several additional dimensions can considerably improve the coherence among reduced bases.

The possibility of creating a typical reduced basis by significantly increasing the dimension of the gathered-subspace has been studied by analyzing the distances among subspaces with different dimensions. In cases with blockage, low-dimensional individual subspaces become closer to the gathered one when the dimension of the gathered subspace increases. Nevertheless, non-blocked cases cannot be really included in the gathered subspace.

Although the results denote some dissimilarities, we perceive that the local POD basis captures abundant physical features in flow fields. Compared to subchannel codes, which only define a single lumped variable in each subdomain, POD basis vectors are possible to represent the 3D flow fields with acceptable accuracy. However, completed implementations, including spatial domain decomposition strategies and the construction of ROMs, need further investigation.

Finally, we address the more technical part: the quantification of the distance among subspaces. Different distances with distinct meanings were utilized. We conclude that all of them are practical to measure distinctions between subspaces and show advantages in specific conditions due to their characteristics. Those considering metrics in all coordinates, like Grassmann, Chordal, Procrustes, and Martin approaches, are preferable for subspaces of high dissimilarities. Asimov, Projection, Spectral, Binet-Cauchy, and Fubini–Study methods emphasize the metric in one direction. Therefore, they are practical to discover the existence of a single quasi-perpendicular coordinate. This is advantageous for subspaces showing a high similarity.

ACKNOWLEDGMENTS

We acknowledge the Framatome Professional School for supporting the research and the China Scholarship Council (CSC) for funding Mr. Shenhui Ruan (CSC student ID: 202106050041) to carry out his doctoral project. Open Access funding enabled and organized by Projekt DEAL.

DATA AVAILABILITY STATEMENT

The data that support the findings of this study are available from the corresponding author upon reasonable request.

ENDNOTES

*The projection matrix of a vector in space Φ is $P = \Phi\left(\Phi^{\mathsf{T}}\Phi\right)^{-1}\Phi^{\mathsf{T}}$. For orthogonal vectors $\Phi^{\mathsf{T}}\Phi = I$, thus $P = \Phi\Phi^{\mathsf{T}}$.

†The absolute error of the projection of a vector a onto a subspace X is given by $E = \left(I - XX^{\mathsf{T}}\right)a$. According to Cauchy–Schwarz inequality, the norm of the normalized projection error $\|e\| = \|\left(I - XX^{\mathsf{T}}\right)a\|/\|a\| \leq \|I - XX^{\mathsf{T}}\|$. Thus *Projection distance* and the difference between the

two projection errors can be connected through the inverse triangular inequality, $\|XX^{\mathsf{T}} - YY^{\mathsf{T}}\|_2 = \|I - YY^{\mathsf{T}} - \left(I - XX^{\mathsf{T}}\right)\|_2 \geq \|I - YY^{\mathsf{T}}\|_2 - \|\left(I - XX^{\mathsf{T}}\right)\|_2$ So *Projection* expression is a measurement related to the difference between 2-norm of normalized projection error of the two subspaces. Chordal manner utilizes the Frobenius norm.

ORCID

Shenhui Ruan https://orcid.org/0009-0006-9046-0220

REFERENCES

1. Stanculescu A. GIF R&D outlook for generation IV nuclear energy systems: 2018 update. Proceedings of the Generation IV International Forum, Paris, France; 2018:16–18.
2. Bertini HW. Descriptions of Selected Accidents that Have Occurred at Nuclear Reactor Facilities. Technical report. Oak Ridge National Lab; 1980.
3. Chai X, Liu X, Xiong J, Cheng X. CFD analysis of flow blockage phenomena in a LBE-cooled 19-pin wire-wrapped rod bundle. *Nucl Eng Des*. 2019;344:107-121.
4. Pacio J, Daubner M, Fellmoser F, Litfin K, Wetzel T. Heat transfer experiment in a partially (internally) blocked 19-rod bundle with wire spacers cooled by LBE. *Nucl Eng Des*. 2018;330:225-240.
5. Yang L, Chen Z, Chen W. Analysis of flow path blockage accident in cased assembly. *Ann Nucl Energy*. 2012;45:8-13.
6. Shi KL, Li SZ, Zhang XL, Zhao PC, Chen HL. Partial flow blockage analysis of the hottest fuel assembly in SNCLFR-100 reactor core. *Nucl Sci Tech*. 2018;29:1-8.
7. Zou X, Zhou T, Zhang G, Jin M, Bai Y. Analysis of core blockage scenarios during pump shutdown accidents for small size lead-cooled fast reactor using RELAP5-HD. *Prog Nuclear Energy*. 2019;111:205-210.
8. Jeong HY, Ha KS, Chang WP, Kwon YM, Lee YB. Modeling of flow blockage in a liquid metal-cooled reactor subassembly with a subchannel analysis code. *Nuclear Technol*. 2005;149(1):71-87.
9. Chang W, Ha K, Suk S, Jeong H. A comparative study of the MATRA-LMR-FB calculation with the SABRE result for the flow blockage accident in the sodium cooled fast reactor. *Nucl Eng Des*. 2011;241(12):5225-5237.
10. Du P, Shan J, Zhang B, Leung LK. Thermal-hydraulics analysis of flow blockage events for fuel assembly in a sodium-cooled fast reactor. *Int J Heat Mass Transf*. 2019;138:496-507.
11. Todreas NE, Kazimi MS. *Nuclear Systems Volume I: Thermal Hydraulic Fundamentals*. CRC Press; 2021.
12. Todreas NE, Kazimi MS, Massoud M. *Nuclear Systems Volume II: Elements of Thermal Hydraulic Design*. CRC Press; 2021.
13. Batta A, Class A. CFD analysis of pressure drop across grid spacers in rod bundles compared to correlations and heavy liquid metal experimental data. *Nucl Eng Des*. 2017;312:121-127.
14. Introini C, Cammi A, Lorenzi S, et al. A 3d CFD model for the study of natural circulation in the Pavia TRIGA Mark II research reactor. Proceedings of the International Conference Nuclear Energy for New Europe (NENE), Bled, Slovenia; 2017:11–14.
15. Chai X, Zhao L, Hu W, et al. Numerical investigation of flow blockage accident in SFR fuel assembly. *Nucl Eng Des*. 2020;359:110437.
16. Introini C, Cammi A. Large-Eddy simulation of the TRIGA mark II reactor Core. Proceedings of the International Conference Nuclear Energy for NewEurope (NENE), Portoroz, Slovenia; 2020:6–9.
17. Crisovan R, Torlo D, Abgrall R, Tokareva S. Model order reduction for parametrized nonlinear hyperbolic problems as an application to uncertainty quantification. *J Comput Appl Math*. 2019;348:466-489.
18. Yanez J, Class AG. Analysis of the accuracy of residual heat removal and natural convection transients in reactor pools. *Nucl Eng Des*. 2021;378:111151.
19. Carere G, Strazzullo M, Ballarin F, Rozza G, Stevenson R. A weighted POD-reduction approach for parametrized PDE-constrained optimal control problems with random inputs and applications to environmental sciences. *Comput Math Appl*. 2021;102:261-276.
20. Nurtaj Hossain M, Ghosh D. Adaptive reduced order modeling for nonlinear dynamical systems through a new a posteriori error estimator: application to uncertainty quantification. *Int J Numer Methods Eng*. 2020;121(15):3417-3441.
21. Rozza G, Stabile G, Ballarin F. *Advanced Reduced Order Methods and Applications in Computational Fluid Dynamics*. SIAM; 2022.
22. Nguyen NC, Peraire J. An efficient reduced-order modeling approach for non-linear parametrized partial differential equations. *Int J Numer Methods Eng*. 2008;76(1):27-55.
23. Amsallem D, Zahr MJ, Farhat C. Nonlinear model order reduction based on local reduced-order bases. *Int J Numer Methods Eng*. 2012;92(10):891-916.
24. Du J, Fang F, Pain CC, Navon I, Zhu J, Ham DA. POD reduced-order unstructured mesh modeling applied to 2D and 3D fluid flow. *Comput Math Appl*. 2013;65(3):362-379.
25. Lorenzi S, Cammi A, Luzzi L, Rozza G. POD-Galerkin method for finite volume approximation of Navier–Stokes and RANS equations. *Comput Methods Appl Mech Eng*. 2016;311:151-179.
26. Stabile G, Hijazi S, Mola A, Lorenzi S, Rozza G. POD-Galerkin reduced order methods for CFD using finite volume discretisation: vortex shedding around a circular cylinder. *Commun Appl Ind Math*. 2017;8(1):210-236.
27. Escanciano JY, Class AG. POD-Galerkin modeling of a heated pool. *Prog Nuclear Energy*. 2019;113:196-205.
28. Shen J, Singler JR, Zhang Y. HDG–POD reduced order model of the heat equation. *J Comput Appl Math*. 2019;362:663-679.

29. Shah NV, Hess MW, Rozza G. Discontinuous Galerkin model order reduction of geometrically parametrized Stokes equation. *Numerical Mathematics and Advanced Applications ENUMATH 2019: European Conference, Egmond aan Zee, The Netherlands, September 30-October 4*. Springer; 2020:551-561.
30. Ferrero A, Iollo A, Larocca F. Global and local POD models for the prediction of compressible flows with DG methods. *Int J Numer Methods Eng*. 2018;116(5):332-357.
31. Riffaud S, Bergmann M, Farhat C, Grimberg S, Iollo A. The DGDD method for reduced-order modeling of conservation laws. *J Comput Phys*. 2021;437:110336.
32. Kaulmann S, Flemisch B, Haasdonk B, Lie KA, Ohlberger M. The localized reduced basis multiscale method for two-phase flows in porous media. *Int J Numer Methods Eng*. 2015;102(5):1018-1040.
33. Ohlberger M, Schindler F. Error control for the localized reduced basis multiscale method with adaptive on-line enrichment. *SIAM J Sci Comput*. 2015;37(6):A2865-A2895.
34. Antonietti PF, Pacciarini P, Quarteroni A. A discontinuous Galerkin reduced basis element method for elliptic problems. *ESAIM Math Model Numer Anal*. 2016;50(2):337-360.
35. Benner P, Schilders W, Grivet-Talocia S, Quarteroni A, Rozza G, Miguel SL. *Model Order Reduction: Volume 2: Snapshot-Based Methods and Algorithms*. De Gruyter; 2020.
36. Xiao D, Fang F, Heaney CE, Navon I, Pain C. A domain decomposition method for the non-intrusive reduced order modelling of fluid flow. *Comput Methods Appl Mech Eng*. 2019;354:307-330.
37. Prusak I, Nonino M, Torlo D, Ballarin F, Rozza G. An optimisation-based domain-decomposition reduced order model for the incompressible Navier-Stokes equations. arXiv preprint arXiv:2211.14528, 2022.
38. Castro dA, Bochev P, Kuberry P, Tezaur I. Explicit synchronous partitioned scheme for coupled reduced order models based on composite reduced bases. arXiv preprint arXiv:2306.05531, 2023.
39. Diaz AN, Choi Y, Heinkenschloss M. A fast and accurate domain-decomposition nonlinear manifold reduced order model. arXiv preprint arXiv:2305.15163, 2023.
40. Diaz AN, Choi Y, Heinkenschloss M. Nonlinear-manifold reduced order models with domain decomposition. arXiv preprint arXiv:2312.00713, 2023.
41. Maday Y, Rønquist EM. A reduced-basis element method. *J Sci Comput*. 2002;17:447-459.
42. Maday Y, Ronquist EM. The reduced basis element method: application to a thermal fin problem. *SIAM J Sci Comput*. 2004;26(1):240-258.
43. Løvgren AE, Maday Y, Rønquist EM. A reduced basis element method for the steady Stokes problem. *ESAIM Math Model Numer Anal*. 2006;40(3):529-552.
44. Iapichino L, Quarteroni A, Rozza G. Reduced basis method and domain decomposition for elliptic problems in networks and complex parametrized geometries. *Comput Math Appl*. 2016;71(1):408-430.
45. Wang H, Planas R, Chandramowlishwaran A, Bostanabad R. Mosaic flows: a transferable deep learning framework for solving PDEs on unseen domains. *Comput Methods Appl Mech Eng*. 2022;389:114424.
46. Taddei T, Xu X, Zhang L. A non-overlapping optimization-based domain decomposition approach to component-based model reduction of incompressible flows. arXiv preprint arXiv:2310.20267, 2023.
47. Smetana K, Taddei T. Localized model reduction for nonlinear elliptic partial differential equations: localized training, partition of unity, and adaptive enrichment. *SIAM J Sci Comput*. 2023;45(3):A1300-A1331.
48. Pegolotti L, Pfaller MR, Marsden AL, Deparis S. Model order reduction of flow based on a modular geometrical approximation of blood vessels. *Comput Methods Appl Mech Eng*. 2021;380:113762.
49. Sambataro G. *Component-Based Model Order Reduction Procedures for Large Scale THM Systems*. PhD Thesis. 2022.
50. Iollo A, Sambataro G, Taddei T. A one-shot overlapping Schwarz method for component-based model reduction: application to nonlinear elasticity. *Comput Methods Appl Mech Eng*. 2023;404:115786.
51. Deza E, Deza MM, Deza MM, Deza E. *Encyclopedia of Distances*. Springer; 2009.
52. Barg A, Nogin DY. Bounds on packings of spheres in the Grassmann manifold. *IEEE Trans Inf Theory*. 2002;48(9):2450-2454.
53. Ye K, Lim LH. Distance between subspaces of different dimensions. arXiv preprint arXiv:1407.0900, 2014.
54. Ye K, Lim LH. Schubert varieties and distances between subspaces of different dimensions. *SIAM J Matrix Anal Appl*. 2016;37(3):1176-1197.
55. Greenshields C. OpenFOAM user guide version v2112; 2021.
56. Moukalled F, Mangani L, Darwish M. *The Finite Volume Method in Computational Fluid Dynamics: An Advanced Introduction with OpenFOAM® and Matlab®*. Springer; 2016.
57. Weller HG, Tabor G, Jasak H, Fureby C. A tensorial approach to computational continuum mechanics using object-oriented techniques. *Comput Phys*. 1998;12(6):620-631.
58. Launder BE, Sharma BI. Application of the energy-dissipation model of turbulence to the calculation of flow near a spinning disc. *Lett Heat Mass Transf*. 1974;1(2):131-137.
59. Versteeg HK, Malalasekera W. *An Introduction to Computational Fluid Dynamics: The Finite Volume Method*. Pearson Education; 2007.
60. Solomenko Z, Haroun Y, Fourati M, Larachi F, Boyer C, Augier F. Liquid spreading in trickle-bed reactors: experiments and numerical simulations using Eulerian–Eulerian two-fluid approach. *Chem Eng Sci*. 2015;126:698-710.
61. Lu X, Xie P, Ingham D, Ma L, Pourkashanian M. A porous media model for CFD simulations of gas-liquid two-phase flow in rotating packed beds. *Chem Eng Sci*. 2018;189:123-134.
62. Landau LD, Lifshitz EM. *Fluid Mechanics: Landau and Lifshitz: Course of Theoretical Physics*. Vol 6. Elsevier; 2013:6.

63. Greenshields C, Weller H. *Notes on Computational Fluid Dynamics: General Principles*. CFD Direct Ltd; 2022.
64. Cheng X. Subchannel analysis for LMR. *Thermal Hydraulics Aspects of Liquid Metal Cooled Nuclear Reactors*. Elsevier; 2019:185-211.
65. Shen D, Liu X, Cheng X. A new turbulent mixing modeling approach for sub-channel analysis code. *Ann Nucl Energy*. 2018;121:194-202.
66. Fazio C, Sobolev V, Aerts A, et al. Handbook on Lead-Bismuth Eutectic alloy and lead properties, materials compatibility, thermal-hydraulics and technologies-2015 edition. Technical report. Organisation for Economic Co-Operation and Development; 2015.
67. Cheng SK, Todreas NE. Hydrodynamic models and correlations for bare and wire-wrapped hexagonal rod bundles—bundle friction factors, subchannel friction factors and mixing parameters. *Nucl Eng Des*. 1986;92(2):227-251.
68. Bubelis E, Schikorr M. *Revised Review and Revised Proposal for Best Fit of Wire-Wrapped Fuel Bundle Friction Factor and Pressure Drop Predictions Using Various Existing Correlations*. Karlsruher Institut für Technologie (KIT); 2016.
69. Benner P, Grivet-Talocia S, Quarteroni A, Rozza G, Schilders W, Silveira LM. *Volume 1 System- and Data-Driven Methods and Algorithms*. De Gruyter; 2021.
70. Quarteroni A, Manzoni A, Negri F. *Reduced Basis Methods for Partial Differential Equations: An Introduction*. Vol 92. Springer; 2015.
71. Afanasiev K, Hinze M. Adaptive control of a wake flow using proper orthogonal decomposition. *Shape Optimization and Optimal Design*. Vol 216. Dekker; 2017:317-332.
72. Lee JM, Lee JM. *Smooth Manifolds*. Springer; 2012.
73. Fortney JP. *A Visual Introduction to Differential Forms and Calculus on Manifolds*. Springer; 2018.

How to cite this article: Ruan S, Yanez J, Class AG. Local reduced subspaces of subchannel-inspired subdomains. *Int J Numer Methods Eng*. 2024;e7552. doi: 10.1002/nme.7552